AGU PUBLICATIONS

Reviews of Geophysics

REVIEW ARTICLE

10.1002/2014RG000461

Key Points:
- Review of (non)conventional techniques for time-frequency representations
- Resolution and performance of nine techniques are tested on five benchmark signals
- Recently developed techniques show clear improvements in most cases

Supporting Information:
- Benchmark signals

Correspondence to:
J. B. Tary,
jean-baptiste.tary@univie.ac.at

Citation:
Tary, J. B., R. H. Herrera, J. Han, and M. van der Baan (2014), Spectral estimation—What is new? What is next?, *Rev. Geophys.*, *52*, doi:10.1002/2014RG000461.

Received 9 MAY 2014
Accepted 18 SEP 2014
Accepted article online 23 SEP 2014

Spectral estimation—What is new? What is next?

Jean Baptiste Tary[1,2], Roberto Henry Herrera[1], Jiajun Han[1], and Mirko van der Baan[1]

[1]Department of Physics, University of Alberta, Edmonton, Alberta, Canada, [2]Now at Department of Meteorology and Geophysics, University of Vienna, Vienna, Austria

Abstract Spectral estimation, and corresponding time-frequency representation for nonstationary signals, is a cornerstone in geophysical signal processing and interpretation. The last 10–15 years have seen the development of many new high-resolution decompositions that are often fundamentally different from Fourier and wavelet transforms. These conventional techniques, like the short-time Fourier transform and the continuous wavelet transform, show some limitations in terms of resolution (localization) due to the trade-off between time and frequency localizations and smearing due to the finite size of the time series of their template. Well-known techniques, like autoregressive methods and basis pursuit, and recently developed techniques, such as empirical mode decomposition and the synchrosqueezing transform, can achieve higher time-frequency localization due to reduced spectral smearing and leakage. We first review the theory of various established and novel techniques, pointing out their assumptions, adaptability, and expected time-frequency localization. We illustrate their performances on a provided collection of benchmark signals, including a laughing voice, a volcano tremor, a microseismic event, and a global earthquake, with the intention to provide a fair comparison of the pros and cons of each method. Finally, their outcomes are discussed and possible avenues for improvements are proposed.

1. Introduction

Spectral or period estimation is a fundamental analysis tool that has a wide range of applications. Accurate and precise analysis of nonstationary spectral variations is a longstanding problem aiming at revealing signal characteristics such as any underlying periodicities. The discrete Fourier transform (DFT) and its fast implementation, the fast Fourier transform (FFT) [*Cooley and Tukey*, 1965; *Cooley et al.*, 1969], and variants have been well studied [e.g., *Hinich and Clay*, 1968; *Brigham*, 1988]. They provide an efficient way to estimate the frequency content of a discrete and finite time series. The main application of the DFT to time-varying spectra is the spectrogram, also called short-time Fourier transform (STFT). Likewise, wavelet transforms and variants are now well-established and many review articles exist [e.g., *Kumar and Foufoula-Georgiou*, 1997; *Mallat*, 2008].

All these methods are bound by the Heisenberg/Gabor uncertainty principle [*Gabor*, 1946] with a trade-off between time and frequency localizations [*Reine et al.*, 2009]. In this review, resolution refers to the ability to resolve two signals close in time or frequency. It includes both localization, which corresponds to the "intrinsic" ability of a technique to separate signals in the *t*–*f* domain, and sampling (see section 2.2 for more explanations). Signal windowing leads to smearing, which corresponds to the widening of the main lobe around its central frequency, as well as sidelobe leakage which introduces spurious frequencies [*Hall*, 2006] (Figure 1). Lately, various new transforms have been developed to ameliorate these issues such as empirical mode decomposition (EMD) coupled with the Hilbert-Huang spectrum [*Huang et al.*, 1998] and the synchrosqueezing transform (SST) [*Daubechies et al.*, 2011].

All the above-mentioned methods can be considered as nonparametric, meaning that they do not assume any particular stationary structure prior to time-frequency (*t*–*f*) decomposition of the signal. On the other hand, parametric methods drew a lot of attention in the 1980s and 1990s as they do not assume zero-valued or periodic data outside the data window and hence are less restricted by smearing and leakage. Autoregressive and autoregressive moving-average models for example provide correct and accurate spectral estimation if the assumed model is appropriate for the investigated time series [*Makhoul*, 1975; *Ulrych and Bishop*, 1975; *Kay and Marple*, 1981].

Here we provide a comprehensive survey of the current state of parametric and nonparametric *t*–*f* transforms including their latest generation. Along the way, we define the time and frequency localization

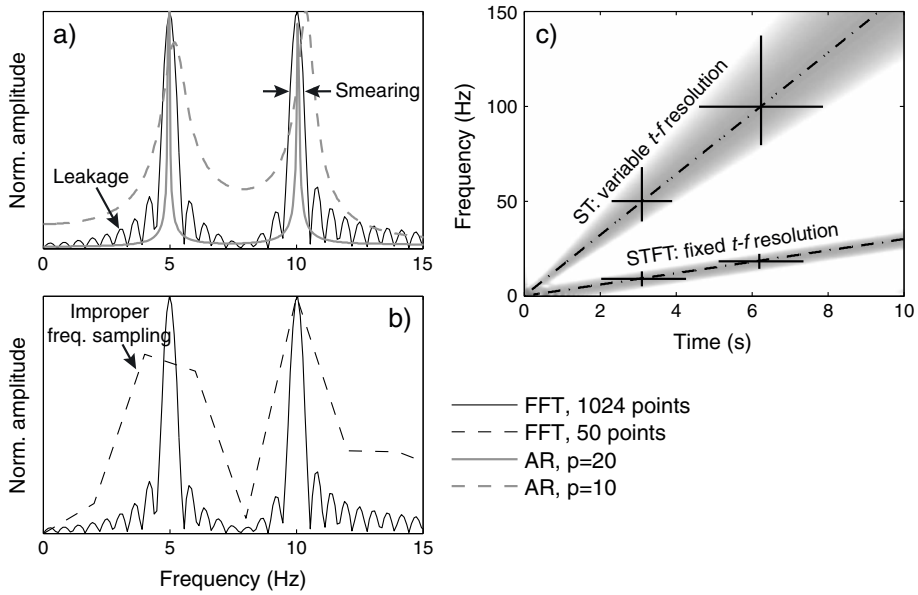

Figure 1. Illustration of (a) spectral smearing and sidelobe leakage and (b) frequency sampling. An untapered signal of 2 s consisting of two sinusoids at 5 and 10 Hz is analyzed using the fast Fourier transform (FFT) and an autoregressive (AR) method (Burg algorithm) [*Burg*, 1972] with different parameters. Contrary to the autoregressive spectrum, the Fourier spectrum with 1024 frequency points shows spectral smearing and sidelobe leakage. The Fourier spectrum with only 50 frequency points does not show correctly the frequencies of the two sinusoids. The influence of the autoregressive order p on t–f localization and accurate frequency determination for autoregressive methods is shown by the two autoregressive spectra with different orders. (c) Two linear chirps of 10 s are analyzed using the short-time Fourier transform (STFT) and S transform (ST) to illustrate the concepts of fixed and variable t–f localization, respectively. The instantaneous frequencies of both chirps are indicated by the dashed-dotted black lines. The short-time Fourier transform, computed using a Hann taper of 0.3 s with 90% overlap, is applied to the chirp with a frequency sweep from 0 to 30 Hz, while the S transform is applied to the chirp with a frequency sweep from 0 to 160 Hz.

of each technique, as well as the difference between spectral resolution, localization, and sample density. We present conventional nonparametric transforms used in geophysical signal processing, i.e., the short-time Fourier transform, the continuous wavelet transform (CWT), and the S transform (ST). We omit the Wigner-Ville distribution because of its main disadvantage: cross-terms without physical meanings that can sometimes mask the true spectral content [*Cohen*, 1989]. We then describe techniques that were developed recently, namely, the synchrosqueezing transform [*Daubechies et al.*, 2011] and empirical mode decomposition and variations [*Huang et al.*, 1998; *Flandrin et al.*, 2004; *Han and van der Baan*, 2013]. Finally, new developments on the estimation of autoregressive models are presented. Within the geoscience community, Kalman filter techniques are mainly employed for time series modeling and forecasting [e.g., *Bertino et al.*, 2003; *Segall et al.*, 2006; *Dikpati et al.*, 2014] and not for spectral estimation.

We describe first their rationale and underlying principles. We then analyze their respective advantages and inconveniences using synthetic, speech, and seismic data to illustrate their distinctive features as well as their complementarities. Even though the presented spectral methods are mainly illustrated on seismic data, most were applied to other fields of earth sciences such as climate time series [*Walker*, 1931; *Torrence and Compo*, 1998; *Ghil et al.*, 2002; *Salisbury and Wimbush*, 2002], hydrology [*Labat*, 2005], ecology [*Cazelles et al.*, 2008], geology [*Bolton et al.*, 1995; *Kravchinsky et al.*, 2013; *Thakur et al.*, 2013; *Reager et al.*, 2014], oceanography [*Farge*, 1992], or solar physics [*Miyahara et al.*, 2006; *Barnhart and Eichinger*, 2011]. Abbreviations and template for each spectral estimation techniques are summarized in Table 1.

2. Methods

2.1. Short-Time Fourier Transform

The Fourier transform is a measure of the similarity of a signal with a family basis formed by sines and cosines. This can be expressed as the inner product of a signal $s(t)$ with a template $\psi(t)$, i.e., $\langle s(t), \psi(t) \rangle = \int_{-\infty}^{\infty} s(t)\psi^*(t)\mathrm{d}t$, where * stands for the complex conjugate [*Gao et al.*, 2010]. When this template is made of

Table 1. Abbreviations, Parametric or Not, and Templates of the *t–f* Techniques Presented in This Review

Techniques	Abbreviation	Parametric	Template
Short-time Fourier transform	STFT	No	Sines and cosines
Continous wavelet transform	CWT	No	Stretched or squeezed, and translated versions of the mother wavelet
S transform	ST	No	Sines and cosines
Synchrosqueezing transform	SST	No	Same as CWT
Matching pursuit	MP	No	User defined dictionary of elementary waveforms
Basis pursuit	BP	No	User defined dictionary of elementary waveforms
Short-time autoregressive method	STAR	Yes	N/A
Kalman smoother	KS	Yes	N/A
Empirical mode decomposition	EMD	No	N/A
Ensemble empirical mode decomposition	EEMD	No	N/A
Complete ensemble empirical mode decomposition	CEEMD	No	N/A

sines and cosines, by Euler's equation for the complex-value cosine $\psi(t) = e^{i2\pi ft}$, the inner product reduces to the Fourier transform

$$FT\{s(t)\} = \langle s(t), e^{i2\pi ft}\rangle = \int_{-\infty}^{\infty} s(t)e^{-i2\pi ft}dt, \quad (1)$$

where t is time, f is frequency, and $i = \sqrt{-1}$.

The Fourier transform is applied to a signal in its entirety and thus assumes stationarity. The short-time Fourier transform is the most popular extension to handle nonstationary time signals. Its easy implementation as well as its good performance explain why this is the most widely used technique for *t–f* representation. Indeed, this is simply the Fourier transform of successive, usually overlapping, windows of the signal, each frequency distribution being associated with the central time of each window. The continuous time short-time Fourier transform can be expressed as

$$S_F(\tau, f) = \int_{-\infty}^{\infty} s(t)w(t-\tau)\, e^{-i2\pi ft}dt, \quad (2)$$

corresponding to the Fourier transform of the signal $s(t)$ tapered by the function $w(t)$, which is usually a Hann or Gaussian function, and where τ is the time delay to the center of the taper. It is easy to see that equation (2) is a special case of equation (1) where we use a tapered window $w(t)$ to select which part of $s(t)$ will be transformed, i.e., $\langle s(t) * w(t), e^{i2\pi ft}\rangle$.

2.2. Time-Frequency Resolution

At this point, it is important to distinguish between time and frequency resolution, localization and sampling (Figure 1). The sample rate in the frequency domain is inversely proportional to the size T of the taper $w(t)$ in the time domain ($\Delta f = 1/T$). There is always the option of zero-padding in the time domain to decrease Δf, improving the readability of the spectrum by increasing the frequency sampling. But well sampled does not mean high resolution [*Kay and Marple*, 1981]. By resolution, we usually mean the ability to distinguish two spectral peaks in a similar way as we do in the time domain to distinguish between two events. Frequency resolution then depends not only on frequency sampling but also on the localization power of each technique. Spectral localization corresponds to the intrinsic ability of each technique to focus individual *t–f* components in the computed *t–f* representations, reducing spectral smearing and sidelobe leakage (Figure 1).

The untapered FFT of a signal is the convolution of a boxcar function with the original time series. The bandwidth of the main lobe of the frequency spectrum of the boxcar function is inversely proportional to the length of the boxcar ($2\pi/T$). The sinc function corresponding to its Fourier transform introduces sidelobes that can mask low-amplitude peaks. The result is a peak smeared around its peak frequency with decaying sidelobes. These effects can be reduced by using tapers such as Hann, Gaussian, or Kaiser-Bessel functions [*Harris*, 1978]. The attenuation of sidelobes is however associated with a widening of the main lobe [*Hall*, 2006]. Spectral smearing can be reduced by enlarging the taper length, yet this reduces the time localization by imposing increased stationarity. Conversely, reducing the taper length improves the time localization at the expense of enhancing spectral smearing, thus lowering spectral localization.

This is known as the Gabor uncertainty principle [*Gabor*, 1946] by analogy with the Heisenberg uncertainty principle in quantum mechanics [*Kumar and Foufoula-Georgiou*, 1997]. The Gabor uncertainty principle tells us that if we define the standard deviation in time and frequency localization by σ_t and σ_f, respectively, then there is a theoretical limit in localization given by [*Hall*, 2006]

$$\sigma_t \sigma_f \geq \frac{1}{4\pi}. \tag{3}$$

For signals $s(t)$ with a duration longer than the taper $w(t)$ support, the fixed length for this taper in the short-time Fourier transform sets the recoverable time and frequency localizations. When the signal's duration is shorter than the support of the taper, then the localization is limited by the signal support itself and not the taper.

Two alternative strategies were developed in the 1980s and 1990s to overcome the undesirable effects introduced by fixed taper lengths for the analysis window $w(t)$ and resulting spectral smearing. Various *t–f* transforms such as the continuous wavelet transform use variable window lengths inversely proportional to the central target frequency (Figure 1). Hence, long windows used for the low frequencies have good frequency but limited time localization, whereas the short windows used for high frequencies have good time but limited frequency localization [*Kumar and Foufoula-Georgiou*, 1997]. The underlying concept is that for short-duration signals, timing errors are relatively more important than errors in frequency content and vice-versa for long-duration signals.

The second strategy is called frequency reassignment and attempts to reduce spectral smearing [*Auger and Flandrin*, 1995; *Han et al.*, 2014]. Temporal and spectral smearing indicates that each *t–f* amplitude is a weighted average of neighboring points in the *t–f* plane. This implies that a nonzero amplitude can be retrieved even if the true signal has no component at this *t–f* pair. The reassignment method computes the sphere of influence of each convolution kernel associated with an analysis window and reallocates the energy in the *t–f* plane to its center of gravity in the time and frequency domains, improving the readability of the *t–f* picture. The reassignment method has also been implemented for other methods such as Wigner-Ville distributions or the continuous wavelet transform [*Auger and Flandrin*, 1995; *Auger et al.*, 2013].

2.3. Continuous Wavelet Transform

The wavelet transform is a well-developed mathematical tool that uses a variable length for the analysis window in equation (2), in contrast to the short-time Fourier transform's fixed length window. Many excellent books and tutorials describe the mathematical foundations of the wavelet transform [*Daubechies*, 1992; *Mallat*, 2008; *Rioul and Vetterli*, 1991; *Torrence and Compo*, 1998]. In this review, for the sake of simplicity and space, we review briefly the rationale and underlying principles to help in the understanding and application of wavelets in geophysical problems.

In the continuous wavelet transform, the analysis taper $w(t)$ is replaced by a mother wavelet ψ that can be shifted in time τ and stretched by a scale a, yielding equation (4).

$$W_s(a,\tau) = \frac{1}{\sqrt{a}} \int_{-\infty}^{\infty} s(t)\, \psi^* \left(\frac{t-\tau}{a} \right) \mathrm{d}t. \tag{4}$$

In other words, $w(t) = \frac{1}{\sqrt{a}}\psi(\frac{t-\tau}{a})$, where the multiplication factor $\frac{1}{\sqrt{a}}$ ensures energy normalization, such that the wavelet always has unit energy at all scales:

$$\int_{-\infty}^{\infty} |\psi_{a,\tau}(t)|^2 \mathrm{d}t = \int_{-\infty}^{\infty} |\psi(t)|^2 \mathrm{d}t = 1, \tag{5}$$

where $\psi(t)$ is the original mother wavelet and $\psi_{a,\tau}(t)$ represents the generated family of translated and scaled wavelets.

A comparison of equations (2) and (4) shows that the continuous wavelet transform shares a similar logic to the short-time Fourier transform; it represents the inner product of the signal with a time shifted and stretched wavelet $\langle s(t), \frac{1}{\sqrt{a}}\psi(\frac{t-\tau}{a})\rangle$. The continuous wavelet transform is simply the cross-correlation of the signal $s(t)$ with a number of wavelets that are scaled and translated versions of the original mother wavelet. $W_s(a,\tau)$ are the coefficients representing a concentrated *t–f* picture. The actual frequency f is built from the central frequency of the mother wavelet f_0 at each scale a with this relation $f = f_0/a$ [*Mallat*

and Zhang, 1993; *Reine et al.*, 2009]. Practical implementations involve the discretization of the scale axis [*Thakur et al.*, 2013].

A mother wavelet (the starting wavelet) is chosen with some specific characteristics in order to improve the signal representation. In all cases, the choice of the wavelet is neither unique nor arbitrary [*Kumar and Foufoula-Georgiou*, 1997]. This template has to satisfy the admissibility condition [*Farge*, 1992; *Daubechies*, 1992], given by

$$C_\psi = 2\pi \int_0^{+\infty} |\omega|^{-1} |\hat{\psi}(\omega)|^2 \mathrm{d}\omega < \infty, \tag{6}$$

where $\hat{\psi}(\omega)$ is the Fourier transform of the mother wavelet $\psi(t)$ and ω is angular frequency. The condition in equation (6) can only be satisfied if the frequency domain wavelet at zero frequency is zero, i.e., $\hat{\psi}(0) = 0$. In other words, the time domain wavelet has zero mean: $\int \psi(t)\mathrm{d}t = 0$.

The wavelet spectrum $\hat{\psi}(\omega)$ should be continuously differentiable, which is validated if the time domain wavelet has a sufficient time decay [*Mallat*, 2008]: $\int_{-\infty}^{\infty}(1 + |t|)|\psi(t)|\mathrm{d}t < +\infty$. This is called the regularity condition. Thus, we have a small waveform that oscillates around zero with equal positive and negative area (i.e., zero mean) and has a short duration, creating a wavelet. The importance of having a wavelet that satisfies the admissibility condition is that the original signal, $s(t)$, can be reconstructed by the inverse wavelet transform.

2.4. *S* Transform

The *S* transform is halfway between the short-time Fourier transform and the continuous wavelet transform. It uses a Gaussian template which is time-shifted by τ and stretched or squeezed by a factor inversely proportional to the linear frequency f [*Stockwell et al.*, 1996]. This is comparable to the mother wavelet used by the continuous wavelet transform, leading *Stockwell et al.* [1996] to describe the *S* transform as a "continuous wavelet transform with a phase shift." The frequency-dependent Gaussian taper is defined by

$$w(t) = \mathrm{e}^{-\frac{t^2}{2\sigma^2}}, \tag{7}$$

where $\sigma = \frac{k}{|f|}$.

Incorporating σ and normalizing the Gaussian taper function lead to the expression for the Gaussian template

$$\hat{w}\left(t, f\right) = \frac{|f|}{k\sqrt{2\pi}} \mathrm{e}^{-\frac{t^2 f^2}{2k^2}}. \tag{8}$$

The parameter k, by controlling the width of the Gaussian taper, can also be tuned to obtain better frequency localization at the expense of reduced time localization. Substituting the Gaussian template for taper $w(t)$ in equation (2), the *S* transform becomes the inner product $\langle s(t) * \frac{|f|}{k\sqrt{2\pi}} \mathrm{e}^{\frac{(t-\tau)^2 f^2}{2k^2}}, \mathrm{e}^{\mathrm{i}2\pi ft} \rangle$, yielding

$$S_{\mathrm{ST}}\left(\tau, f\right) = \frac{|f|}{k\sqrt{2\pi}} \int_{-\infty}^{\infty} s(t) \mathrm{e}^{\frac{-(t-\tau)^2 f^2}{2k^2}} \mathrm{e}^{-\mathrm{i}2\pi ft} \mathrm{d}t. \tag{9}$$

Like the continuous wavelet transform, the *t*–*f* localization of the *S* transform is variable (Figure 1). The variable *t*–*f* localization of the *S* transform and continuous wavelet transform enables the analysis of signals with frequency components separated by few orders of magnitude (e.g., 1 and 1000 Hz).

Unlike the continuous wavelet transform, the *S* transform keeps the properties of the Fourier transform such as a uniform frequency sampling, spectral amplitudes independent of frequency owing to the normalization of the Gaussian taper to unit area in equation (9), and retains the original signal phase [*Stockwell*, 2007]. On the other hand, the continuous wavelet transform is characterized by an exponential scale sampling (i.e., more scales are allocated on lower portions than higher portions of the spectrum, producing an equal number of scales per octave instead of a linear frequency sampling), "locally defined" phase, and show higher amplitudes at lower frequencies.

2.5. Synchrosqueezing Transform

The synchrosqueezing transform is a derivation of the continuous wavelet transform empowered by a reassignment step [*Daubechies et al.*, 2011]. It concentrates the frequency content around the instantaneous frequencies in the wavelet domain. The synchrosqueezing transform assumes that the signal $s(t)$ is the sum of individual time-varying harmonic components:

$$s(t) = \sum_{k=1}^{K} A_k(t)\cos(\theta_k(t)) + \eta(t), \tag{10}$$

where $A_k(t)$ is the instantaneous amplitude and $f_k(t) = \frac{1}{2\pi}\frac{\mathrm{d}}{\mathrm{d}t}\theta_k(t)$ is the instantaneous frequency of the signal component k, derived from the instantaneous phase $\theta_k(t)$. The additive noise $\eta(t)$ includes the contribution of environmental and acquisition sources, and K stands for the maximum number of components in the signal. This is a mathematical simplification, but this will enable signal separation and analysis.

The rationale behind this technique is that concentrating the t–f map into the most representative instantaneous frequencies will decrease smearing while still allowing reconstruction. With the continuous wavelet transform, the variable length of the mother wavelet leads to a more flexible trade-off between time and frequency localization but does not prevent spectral smearing in the t–f plane. *Daubechies et al.* [2011] observed that there is a physical limit to reduce the smearing effect in the t–f representation using the continuous wavelet transform. This smearing mainly occurs along scale axis; thus, if we want to get frequency variations with time, we need to compute the instantaneous frequencies also in the wavelet domain. The angular instantaneous frequency is the rate of change of the time-dependent phase ($\omega(t) = \frac{\mathrm{d}\theta(t)}{\mathrm{d}t}$) [*Taner et al.*, 1979]; likewise in the wavelet domain, the instantaneous frequency $\omega_s(a,\tau)$ is computed as the derivative of the wavelet transform at any point (a,τ) with respect to τ, for all $W_s(a,\tau) \neq 0$:

$$\omega_s(a,\tau) = \frac{-\mathrm{i}}{2\pi W_s(a,\tau)}\frac{\partial W_s(a,\tau)}{\partial \tau}. \tag{11}$$

The instantaneous frequencies are the ridges in the t–f representation [*Auger et al.*, 2013]. To decrease the smearing, we have to squeeze the frequencies around these ridges. This is to map the information from the time-scale plane to the t–f plane. Every point (a,τ) is converted to $(\omega_s(a,\tau),\tau)$, and this operation is called synchrosqueezing [*Daubechies et al.*, 2011]. Since the scale a and time τ are discrete values, we can have a scaling step $\Delta a_k = a_{k-1} - a_k$ for any a_k where $W_s(a,\tau)$ is computed. Likewise, when mapping from the time-scale plane to the t–f plane $(a,\tau) \rightarrow (\omega(a,\tau),\tau)$, the synchrosqueezing transform $T_s(\omega,\tau)$ is determined only at the centers ω_l of the frequency range $[\omega_l - \Delta\omega/2, \omega_l + \Delta\omega/2]$, with $\Delta\omega = \omega_l - \omega_{l-1}$:

$$T_s(\omega_l,\tau) = \frac{1}{\Delta\omega}\sum_{a_k} W_s(a_k,\tau)a^{-3/2}\Delta a_k. \tag{12}$$

where the scale a_k is bounded by $|\omega(a_k,\tau) - \omega_l| \leq \Delta\omega/2$. This means that a small frequency band centered at ω_l and less than half of the bandwidth is used to reconstruct the concentrated frequency map at time τ. The new t–f representation of the signal $T_s(\omega_l,\tau)$ is synchrosqueezed along the frequency (or scale) axis only [*Li and Liang*, 2012].

The discretized version of $T_s(\omega_l,\tau)$ in equation (12) is represented by $\tilde{T}_{\tilde{s}}(w_l,t_m)$, where t_m is the discrete time $t_m = t_0 + m\Delta t$ with Δt the sampling interval, $m = 0,\ldots,n-1$ and n is the total number of samples in the discrete signal $\tilde{s}_m$. The frequency localization in the synchrosqueezing transform is also limited by the Gabor uncertainty principle. The Nyquist theorem gives the upper frequency limit $\mathrm{f}_{\max} = 1/(2\Delta t)$ and the minimum frequency is $\mathrm{f}_{\min} = 1/(n\Delta t)$, with n the signal length. With these two bounds, the synchrosqueezing transform discretizes the scale axis to compute the frequency division step ω_l. More special considerations are described in *Thakur et al.* [2013].

Summing up the previous steps, the synchrosqueezing transform assumes that the signal is a superposition of nonstationary monochromatic wavelets and can be efficiently decomposed by the continuous wavelet transform, followed by the computation of the instantaneous frequencies plus a reassignment step to concentrate the energy around the ridges. An extended explanation with applications to seismic signals can be found in *Herrera et al.* [2014].

The reconstruction of the individual components s_k from the discrete synchrosqueezed transform $\tilde{T}_{\tilde{s}}$ is then the inverse continuous wavelet transform over a small frequency band $l\epsilon L_k(t_m)$ around the k_{th} component:

$$s_k(t_m) = 2C_\psi^{-1}\Re\left(\sum_{l\epsilon L_k(t_m)} \tilde{T}_{\tilde{s}}(w_l, t_m)\right), \tag{13}$$

where C_ψ is a constant dependent on the selected wavelet. As we take the real part $\Re$ of the discrete synchrosqueezing transform in that band, we recover the real component s_k. In this review, we follow *Thakur et al.* [2013] where the reconstruction is done by a standard least-squares ridge extraction method.

2.6. Matching Pursuit

In the matching pursuit (MP) algorithm, the signal is decomposed into waveforms selected from a dictionary of *t–f* atoms [*Mallat and Zhang*, 1993]. Time-frequency atoms are discrete-time elementary waveforms populating the dictionary. This technique assumes that the signal is a linear combination of these atoms from a dictionary that is not necessarily built with modulated sine and cosine waves atoms. Matching pursuit uses a recognition step to identify and subsequently remove the most prominent atom via a deflationary approach and then repeats the recognition step [*Chen et al.*, 2001]. The subtraction step prevents smearing and leakage, creating highly localized *t–f* decompositions.

Generally, the *t–f* atoms are the dilations, translations, and modulations of a single window function:

$$\psi_\gamma(t) = \frac{1}{\sqrt{a}}\psi\left(\frac{t-\tau}{a}\right)e^{i\omega(t-\tau)}, \tag{14}$$

where $\gamma = (a, \omega, \tau)$, i.e., the three transformations scale, modulation, and translation, respectively. Thus, the recognition step of matching pursuit comprises the inner product of the signal $s(t)$ and then the residual signal $R^{(n)}s$ which is the original signal minus any subtracted wavelets, with a time shifted, stretched, and modulated wavelet, i.e., $\langle s(t), \psi_\gamma(t)\rangle$ or $\langle R^{(n)}s, \psi_\gamma(t)\rangle$.

Mallat and Zhang [1993] proposed to build a dictionary D, with an entire set of waveforms ψ_γ, in order to best match the signal structures. Matching pursuit uses a greedy algorithm, which means that at each iteration it chooses a waveform from the dictionary that is best adapted to the signal segment under analysis and repeats this operation until a predefined stopping criterion is reached. This produces a sparse representation of the signal, $s(t)$, as the weighted sum of chosen waveforms (ψ_γ), picked up from the dictionary D [*Wang*, 2007]:

$$s(t) = \sum_{n=0}^{N-1} a_n \psi_{\gamma_n}(t) + R^{(n)}s, \tag{15}$$

where N is the total number of iterations, a_n is the amplitude of the wavelet ψ_{γ_n}, and $R^{(n)}s$ is the residual at iteration n, with $R^0 s = s$.

Dictionaries are built with different waveforms $D = \{\psi_\gamma\}_{\psi\in D}$. The user determines the extent of the dictionary and the type of waveforms used. A large dictionary allows for a more complete signal representation but at the expense of significantly longer computation times. If the waveforms are sines and cosines, then it is a Fourier dictionary and the representation is analogous to a "sparse Fourier transform." If a wavelet dictionary is built from a mother wavelet, then the representation becomes analogous to a "sparse continuous wavelet transform." On the other hand, a *t–f* dictionary, also known as Gabor dictionary [*Mallat and Zhang*, 1993], produces a decomposition of the signal $s(t)$ into *t–f* atoms. Computing the Wigner distribution of each atom leads to the *t–f* representation [*Mallat and Zhang*, 1993]. Matching pursuit may lead to similar time-frequency representations compared with the previous techniques, but its deflationary approach prevents spectral leakage, thereby creating a much sparser representation. Unlike the previous methods, the matching pursuit algorithm is not exploring the complete *t–f* plane but is mapping *t–f* atoms located at the positions of maximum residual reduction [*Addison*, 2002].

2.7. Basis Pursuit

The main principle of basis pursuit (BP) is similar to that of matching pursuit as it seeks to decompose a signal into individual atoms from a predefined dictionary, yet with two important differences. First, it includes a minimization term to reduce the number and magnitudes of retrieved atoms, yielding a sparse representation [e.g., *Chen et al.*, 2001]. Second, instead of applying a deflationary approach where atoms are

recognized and removed sequentially, basis pursuit identifies all atoms simultaneously by casting both steps into a single inversion problem [*Bonar and Sacchi*, 2010; *Zhang and Castagna*, 2011; *Vera Rodriguez et al.*, 2012].

The signal $s(t)$ is represented as the convolution of a family of wavelets $\psi(t,n)$ and its associated coefficient series $a(t,n)$ as

$$s(t) = \sum_{n=1}^{N} [\psi(t,n) * a(t,n)]. \tag{16}$$

where N is the number of atoms, t is time, and n is the dilation of atom $\psi(t,n)$ determining its frequency. Using matrix notation, equation (16) can be rewritten as

$$\mathbf{s} = (\mathbf{\Psi_1} \quad \mathbf{\Psi_2} \quad \ldots \quad \mathbf{\Psi_N}) \begin{pmatrix} a_1 \\ a_2 \\ \vdots \\ a_N \end{pmatrix} + \boldsymbol{\eta} = D\mathbf{a} + \boldsymbol{\eta}. \tag{17}$$

where $\mathbf{\Psi_n}$ denotes the convolution matrix of $\psi(t,n)$ with dilation index n, D is the wavelet dictionary, and $\boldsymbol{\eta}$ is the noise. The t–f distribution of basis pursuit corresponds then to the set of weights $\mathbf{a}$ associated with the set of atoms $\psi(t,n)$ coming from the dictionary D [*Chen et al.*, 2001].

At this point, two options are possible, namely, a perfect or a sparse approximate decomposition [*Chen et al.*, 2001; *Vera Rodriguez et al.*, 2012]. The latter is also known as basis pursuit denoising. In the first case, one solves the problem: minimize $||\mathbf{a}||_1$ subject to $D\mathbf{a} = \mathbf{s}$, where $||.||_1$ indicates the ℓ_1 norm (i.e., minimum of absolute numbers). In the second case, one minimizes

$$J = \frac{1}{2}||\mathbf{s} - D\mathbf{a}||_2^2 + \lambda||\mathbf{a}||_1. \tag{18}$$

The first term of cost function J represents the data misfit term based on the ℓ_2 norm, that is, the least-squares difference between the observed and predicted data, whereas the second term of J is the regularization term, based on the ℓ_1 norm. λ is the trade-off parameter controlling the relative strength between the data misfit and the number of nonzero coefficients $\mathbf{a}$. A variety of solvers exist to obtain a solution to equation (18) [*Figueiredo et al.*, 2007; *van den Berg and Friedlander*, 2008; *Beck and Teboulle*, 2009].

Unlike matching pursuit, basis pursuit is not a greedy algorithm. It starts from an initial model and iteratively improves the model by swapping wavelets from the predefined dictionary. Basis pursuit converges eventually to a local optimum which is not guaranteed for matching pursuit [*Chen et al.*, 2001].

The performance of matching pursuit and basis pursuit is strongly dependent on the predefined wavelet dictionary. Combining different dictionaries to make bigger, more complete dictionaries can enhance basis pursuit decompositions [*Chen et al.*, 2001; *Rubinstein et al.*, 2010] but comes at the expense of making matrix D bigger and thus prolonging computation time.

The techniques presented in the next sections, corresponding to autoregressive methods and empirical mode decomposition and variants, are fundamentally different from the previous ones as they drop the comparison with a template performed by an inner product of signal and basis functions.

2.8. Autoregressive Methods

Autoregressive methods for periodicity analysis were introduced by G. U. Yule and G. Walker in the first half of the twentieth century and applied to environmental time series [*Yule*, 1927; *Walker*, 1931]. Linear autoregression, in combination with a moving average scheme, was then used to forecast the values of economic time series such as price indices [*Wold*, 1938]. The fundamental idea of autoregressive models is to reduce a time series to a small set of parameters. Autoregressive methods are called linear prediction filters because they use a set of past values to estimate the future ones. This has important implications for the resulting frequency localization as the signal is not strictly windowed like FFT-based methods. This is the reason why the frequency localization of autoregressive methods sometimes seems to "violate the uncertainty principle" [*Marple*, 1982]. Using the autoregressive coefficients, specific parts of the signal can then be reconstructed.

Autoregressive models consider a time series s_n as a weighted sum of p past values driven by a white noise process v_n following

$$s_n = \sum_{k=1}^{p} a^k s_{n-k} + v_n, \tag{19}$$

where n are the time steps, a^k are the coefficients of the autoregressive model of order p, and v_n is a random white noise process with zero mean and variance σ_s^2.

The power spectrum of an autoregressive filter is then given by

$$S_A(f) = \frac{{\sigma_s}^2}{\left|1 - \sum_{k=1}^{p} a^k e^{-i2\pi kf/f_s}\right|^2}, \tag{20}$$

where f_s is the sampling frequency.

Except for the method to obtain the autoregressive coefficients, the main parameter of autoregressive models is the order of the filter p. The signal window length has only one main restriction: it should be longer than twice the autoregressive order [*Ulrych and Ooe*, 1983]. The number of coefficients has a critical influence on the estimated spectrum as it sets the number of recoverable frequencies independent of signal $s(t)$. For the different applications, we use a grid-search algorithm to find the minimum in a least-squares sense of the spectral comparison between Fourier and autoregressive spectra to determine the optimum autoregressive order [*Tary et al.*, 2014].

As autoregressive models are all-pole filters, they are characterized by peaked spectra. Therefore, only signals with such spectra should be good candidates for this method [*Kay and Marple*, 1981]. The poles defining autoregressive filters correspond to the different modes of a resonator. In the following sections, we will describe two different autoregressive methods able to capture time-varying frequency content.

2.8.1. Short-Time Autoregressive Method

As the name suggests, the short-time autoregressive method (STAR) is an application of autoregressive models on short windows. Like the short-time Fourier transform, the short-time autoregressive method deals with nonstationary spectra by assuming that signals are piecewise stationary in short, untapered windows. The autoregressive spectrum, calculated from the autoregressive coefficients determined using the Burg method [*Burg*, 1972] and equation (20), is computed for short, overlapping windows and then merged sequentially to obtain the final picture. The time localization is then the same as the short-time Fourier transform but is independent of the frequency localization, although the maximum autoregressive order p is still limited by the window length. The frequency localization depends mainly on the signal-to-noise ratio and the autoregressive order [*Marple*, 1982; *Quirk and Liu*, 1983], even though spectral estimates using the Burg method employ the total data window [e.g., *Muthuswamy and Thakor*, 1998].

2.8.2. Continuous Autoregressive Model: Kalman Smoother

Rather than assuming stationarity in short windows, one can modify equation (19) to use time-varying autoregressive coefficients defined at each time step n,

$$s_n = \sum_{k=1}^{p} a_n^k s_{n-k} + v_n, \tag{21}$$

where a_n^k are the nonstationary autoregressive coefficients.

The nonstationary coefficients are usually determined using stochastic or deterministic regression methods [*Kaipio and Karjalainen*, 1997]. For the deterministic method, a set of basis functions with variable amplitudes is used in order to model the time-varying frequency content [e.g., *Hall et al.*, 1983]. In the case of stochastic methods, a recursive algorithm is generally employed to determine the autoregressive coefficients at instant n from the autoregressive coefficients at instant $n-1$ [e.g., *Baziw and Weir-Jones*, 2002]. In the following, we present a stochastic method, the Kalman smoother (KS) [*Khan and Dutt*, 2007; *Tary et al.*, 2014].

The autoregressive model assumes that the observation at instant n, y_n, is a linear combination of a vector of previous measurements $\mathbf{m}_n$ weighted by the vector of autoregressive coefficients $\mathbf{x}_n$, also called the state vector, plus some random noise ε_n. The measurement equation is then

$$s_n = \mathbf{m}_n^{'}\mathbf{x}_n + \varepsilon_n, \tag{22}$$

where the prime denotes matrix transpose.

The Kalman filter uses a recursive scheme to predict the next estimate from the previous one. The state variable at instant n, $\mathbf{x}_n$, is then obtained from the state variable at $n-1$, $\mathbf{x}_{n-1}$, by the transition equation

$$\mathbf{x}_n = T\mathbf{x}_{n-1} + \boldsymbol{\eta}_n, \tag{23}$$

where T is the state transition matrix and $\boldsymbol{\eta}_n$ is the state noise. In addition, the following assumptions are made

1. The measurement and state noises are independent, white noise processes which are normally distributed with zero mean and known covariance matrices.
2. The state vector $\mathbf{x}_n$ is a Gauss-Markov process independent on both measurement and state noises.
3. The initial state is defined by its mean $\boldsymbol{\mu}_{0|0}$ and covariance matrix $P_{0|0}$, given by

$$\begin{aligned} \boldsymbol{\mu}_{0|0} &= E\left[\mathbf{x}_0\right], \\ P_{0|0} &= E\left[\left(\mathbf{x}_0 - \hat{\mathbf{x}}_{0|0}\right)\left(\mathbf{x}_0 - \hat{\mathbf{x}}_{0|0}\right)'\right], \end{aligned} \tag{24}$$

where the hat refers to estimates, $E[\cdot]$ is the mathematical expectation, and the notation $\boldsymbol{\mu}_{n|n-1}$ corresponds to the estimate at time step n given the estimates at $n-1$. Initial estimates for $\boldsymbol{\mu}_{0|0}$, $P_{0|0}$ and $\hat{\mathbf{x}}_{0|0}$ are generally obtained using a training data set [*Tary et al.*, 2014].

Optimal estimates of the state vector are obtained by minimizing the covariance of the estimates at the instant $n+1$ given the set of observations $\mathbf{s}_{1:n+1} = [s_1, \ldots, s_{n+1}]$. This is achieved by using the prediction and update equations for the Kalman filter [*Grewal and Andrews*, 2001]. The estimates of the state vector can be further smoothed by applying the Rauch-Tung-Striebel backward recursions [*Rauch et al.*, 1965]. Using the forward recursions of the Kalman filter together with the smoothing backward recursions corresponds to the Kalman smoother. Additional details on this algorithm can be found in *Tary et al.* [2014].

2.9. Empirical Mode Decomposition and Variants

Empirical mode decomposition, developed by *Huang et al.* [1998], is a powerful signal analysis technique to model nonstationary and nonlinear signal systems. Through the extraction of intrinsic mode functions (IMFs), empirical mode decomposition captures the nonstationary feature of seismic data. A t–f representation is obtained by combining empirical mode decomposition with the Hilbert transform to compute instantaneous frequencies [*Taner et al.*, 1979; *Magrin-Chagnolleau and Baraniuk*, 1999]. This is sometimes called the Hilbert-Huang spectrum [*Huang et al.*, 1998].

The instantaneous frequency [*Taner et al.*, 1979] holds the promise of the highest possible time localization since it produces a frequency at each time sample, but at the expense of a very limited frequency localization, due to the Gabor uncertainty principle, equation (3). This often leads to rapid fluctuations from time sample to time sample. In addition, it can even produce negative frequencies which hold uncertain physical meaning. Instantaneous frequency is thus a somewhat controversial variable [*Barnes*, 2007; *Fomel*, 2007; *Han and van der Baan*, 2013]. Empirical mode decomposition aims at solving the predicament of instantaneous frequency, as each IMF after decomposition is guaranteed to be a symmetric, narrow-band waveform, which ensures that the instantaneous frequency of each IMF is smooth and positive.

The IMFs are computed recursively, starting with the most oscillatory one. The decomposition method uses the envelopes defined by the local maxima and minima of the input seismic trace. Once the maxima of the original signal are identified, a spline is used to interpolate all the local maxima and construct the upper envelope. The same procedure is used for local minima to obtain the lower envelope. The mean of the upper and lower envelopes is then subtracted from the initial signal. This interpolation process is pursued on the remaining signal. This procedure is called sifting, and it terminates when the mean envelope is reasonably close to zero everywhere. The resultant signal is designated as the first IMF.

The first IMF is then subtracted from the data, and the difference is treated as a new signal on which the same sifting procedure is applied to calculate the next IMF. The decomposition is stopped when the last IMF has a small amplitude or becomes monotonic [*Huang et al.*, 1998; *Bekara and Van der Baan*, 2009; *Han and van der Baan*, 2013]. As the name implies, empirical mode decomposition is an empirical decomposition in that no *a priori* decomposition basis is chosen such as sines and cosines for the Fourier transform or a mother wavelet for the Wavelet transform.

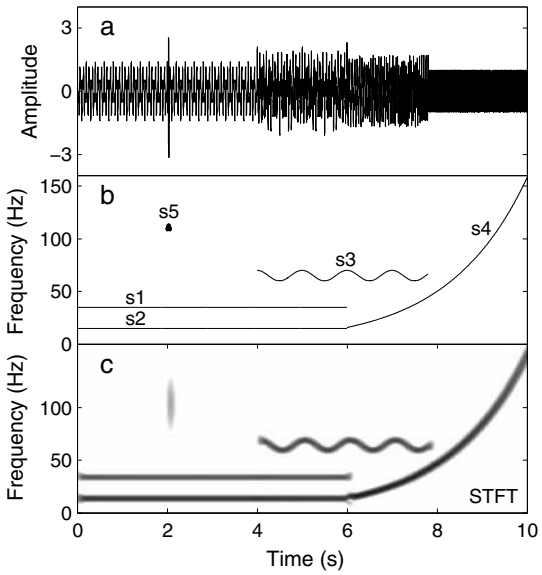

Figure 2. Synthetic signal constituted by straight, frequency-modulated, and gliding harmonic components and one Morlet wavelet. (a) Time series. (b) Instantaneous frequencies (see text for equations corresponding to the signal labels). (c) Short-time Fourier transform (STFT) computed using a Hann taper of 0.4 s with 90% overlap.

Empirical mode decomposition has several interesting properties that makes it an attractive tool for signal analysis. It results in complete signal decomposition; i.e., the original signal is reconstructed by summing all IMFs. No loss of information is incurred. The empirical mode decomposition is a quasi-orthogonal decomposition in that the cross-correlation coefficients between the different IMFs are always close to zero. This minimizes energy leakage between the IMFs [*Bekara and Van der Baan*, 2009].

Even though empirical mode decomposition offers several promising properties, some features encumber its direct application: mode mixing and splitting, aliasing, and end-point artefacts [*Mandic et al.*, 2013]. Empirical mode decomposition is also relatively inefficient for flat signals due to the extrema interpolation step and for signals with frequency components that are not well-separated.

Two variants were recently introduced to overcome some of the negative features associated with empirical mode decomposition, namely, ensemble empirical mode decomposition (EEMD) and complete ensemble empirical mode decomposition (CEEMD). Ensemble empirical mode decomposition, briefly speaking, is empirical mode decomposition combined with noise stabilization. Using the injection of controlled zero mean, Gaussian white noise, ensemble empirical mode decomposition effectively reduces mode mixing [*Wu and Huang*, 2009; *Tong et al.*, 2012; *Mandic et al.*, 2013]. Adding white Gaussian noise helps perturb the signal and enables the empirical mode decomposition algorithm to visit all possible solutions in the finite neighborhood of the final answer, and it also takes advantage of the zero mean of the noise to cancel aliasing [*Wu and Huang*, 2009]. However, ensemble empirical mode decomposition leaves two problems: first, different noise realizations may end up with different numbers of IMFs, which could mix up the IMFs after each decomposition in the frequency domain; second, ensemble empirical mode decomposition does not maintain the complete decomposition feature of empirical mode decomposition [*Torres et al.*, 2011; *Han and van der Baan*, 2013]. In other words, contrary to empirical mode decomposition, the sum of the IMFs obtained via ensemble empirical mode decomposition does not necessarily reconstruct the original signal. The reconstruction error of ensemble empirical mode decomposition is often acceptable when the injected noise is of small amplitude.

An important improvement of ensemble empirical mode decomposition is complete ensemble empirical mode decomposition, proposed by *Torres et al.* [2011], which obtains again the final IMFs sequentially, contrary to ensemble empirical mode decomposition. The first IMF component is obtained in the same way as ensemble empirical mode decomposition. The next IMF components can be calculated by the following equation:

$$\mathrm{IMF}_{(k+1)} = \frac{1}{N}\sum_{n=1}^{N} E_1[r_k + \xi E_k[v_n]]. \tag{25}$$

where E_k is the empirical mode decomposition operator which produces the k-th IMF component, r_k is the k-th decomposition residue, ξ is a fixed percentage of injected Gaussian white noise v_n, and N is the number of realizations. Complete ensemble empirical mode decomposition is a robust extension of empirical mode decomposition methods. It leads to complete signal reconstructions.

The properties of empirical mode decomposition and its variants are not fully understood. In particular, its exact time and frequency localizations are not predictable, although *Han and van der Baan* [2013] provide

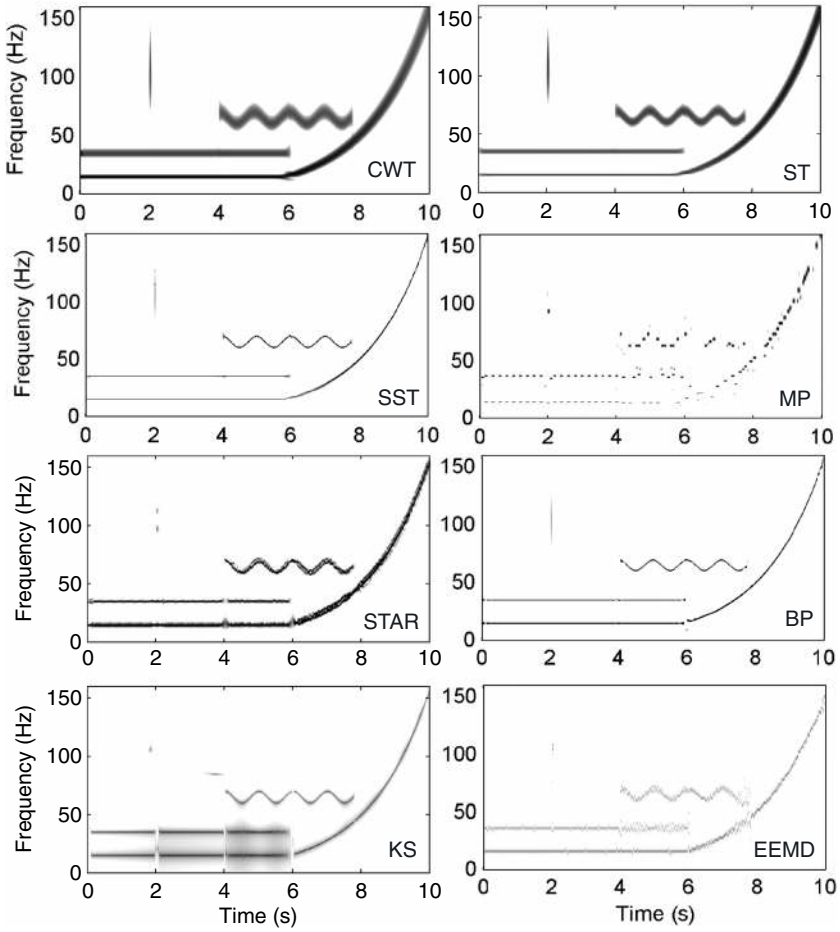

Figure 3. Time-frequency representations of the synthetic signal of Figure 2 using the ST, STAR, KS, CWT, SST, EMD, BP, and MP. The different techniques are computed using the following parameters: ST, parameter k=10; STAR, window of 0.3 s with 90% overlap and an autoregressive order of 21; KS, autoregressive order of 21; CWT and SST, Morlet wavelet with 64 voices per octave; EEMD, 100 realizations and random noise injection with 10% of the signal maximum amplitude; MP, Gabor dictionary; BP, Morlet wavelet dictionary; and regularization parameter λ=0.5.

some hypotheses. Given the uncertainty principle, the instantaneous frequency produces the highest possible time localization at each time sample, which necessarily comes along with poor frequency localization. Based on the constant-Q band-pass feature of empirical mode decomposition [*Flandrin et al.*, 2004], ensemble empirical mode decomposition and complete ensemble empirical mode decomposition extract the IMFs in each octave more accurately with the help of noise stabilization. The inherent frequency localization of each individual IMF, given a white-noise input signal, is one octave with a time localization inversely proportional to the center frequency of this octave. With increasing IMFs, each octave is centered around a decreasing base frequency with a narrower linear frequency range. The obtained IMFs thus have an increasing frequency localization at the expense of a decreasing time localization. In other words, the first IMF has the highest time localization and the lowest frequency localization, and vice-versa for the last IMF.

3. Applications

For each benchmark signal, the important parameters used with each technique are mentioned in the caption of the figures.

3.1. Toy Examples

3.1.1. Synthetic Example

In order to test the performances of the aforementioned techniques on a noise-free signal, we build a synthetic signal, shown in Figure 2, consisting of two harmonic components at 15 and 35 Hz ($s1$ and $s2$),

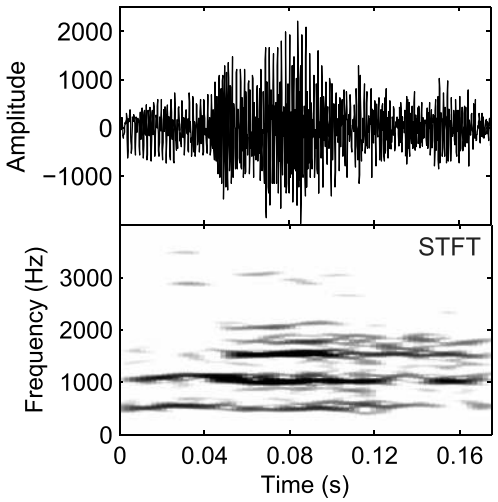

Figure 4. Speech signal corresponding to a sample of a voice laughing and its time-frequency representation using the STFT. The STFT is computed using a Hann taper of 0.025 s with 90% overlap.

one frequency-modulated harmonic around 65 Hz (*s*3), one harmonic gliding from 15 to 158 Hz (*s*4), and one Morlet wavelet with a central frequency of ~113 Hz (*s*5). The equations and associated instantaneous frequencies (IF, in brackets) corresponding to these components are

$$s1(t) = 0.6\cos(70\pi t) \quad [\mathrm{IF}:35]$$

$$s2(t) = 0.8\cos(30\pi t) \quad [\mathrm{IF}:15]$$

$$s3(t) = 0.7\cos(130\pi t + 5\sin(2\pi t)) \quad [\mathrm{IF}: 65 + 5\cos(2\pi t)]$$

$$s4(t) = \sin\left(\frac{8\pi 100^{\frac{t}{8}}}{\ln(100)}\right) \quad [\mathrm{IF}:\frac{100^{\frac{t}{8}}}{2}]$$

$$s5(t) = 3\exp\left(\frac{-t^2}{2}\right)\cos(5t) \quad [\mathrm{IF}:\frac{5}{2\pi}\frac{\mathrm{f_s}}{\log_2(N_5)} - |t|]$$

where instantaneous frequencies are calculated as $\frac{1}{2\pi}\frac{\mathrm{d}\phi(t)}{\mathrm{d}t}$ with $\phi(t)$ the argument of the signal components, ln and $\log_2$ are the natural and binary logarithms, respectively, N_5 is the number of samples of signal *s*5, and $\mathrm{f_s}$ is the sampling frequency.

This synthetic signal includes straight, frequency-modulated, sharp, and progressive changes in spectral lines, as well as a Morlet wavelet with localized *t*–*f* support. The decomposition results for all techniques are presented in Figure 3.

The *t*–*f* representations of this noise-free synthetic signal clearly shows the expected performances of the conventional techniques: short-time Fourier transform (STFT), continuous wavelet transform (CWT), and *S* transform (ST). Spectral lines for the short-time Fourier transform have a constant width, reflecting the fixed *t*–*f* localization of this method, while the variable *t*–*f* localization of the continuous wavelet transform and *S* transform involves the widening of the spectral lines toward higher frequencies together with the better temporal localization of the high-frequency Morlet atom. Both the short-time Fourier transform and *S* transform seem to retain the amplitude of the different components, unlike the continuous wavelet transform which show a decrease in maximum amplitude toward higher frequencies due to the frequency widening of the wavelet support and the wavelet energy conservation required by this technique.

The autoregressive techniques (short-time autoregressive method STAR and Kalman Smoother KS), basis pursuit (BP), synchrosqueezing transform (SST), and ensemble empirical mode decomposition (EEMD) show higher *t*–*f* localizations close to the theoretical instantaneous frequencies, with the exception of short-time autoregressive method and ensemble empirical mode decomposition which exhibits somewhat noisy frequency components for those varying over time. Ensemble empirical mode decomposition maps the continuous spectrum of the Morlet atom to a single point, contrary to the more conventional methods. Like autoregressive methods, empirical mode decomposition is challenged when handling continuous spectra [e.g., *Kay and Marple*, 1981]. Even though the localization of this atom is fully recovered by the Kalman smoother, its time position is slightly shifted due to some smoothing. The *t*–*f* smoothing also leads to the introduction of spurious components such as the one at ~80 Hz and 3.9 s. The separation of the Morlet atom into two spectral peaks by the short-time autoregressive method illustrates another pitfall of autoregressive methods, which is spectral line splitting. Splitting occurs essentially for high autoregressive orders, compared to the number of frequency components in the signal, and noise-free signals [*Chen and Stegen*, 1974; *Kay and Marple*, 1979]. In this case, the presence of small amplitude noise would be beneficial, as it prevents allocation of multiple autoregressive coefficients to higher amplitude spectral peaks. Additional

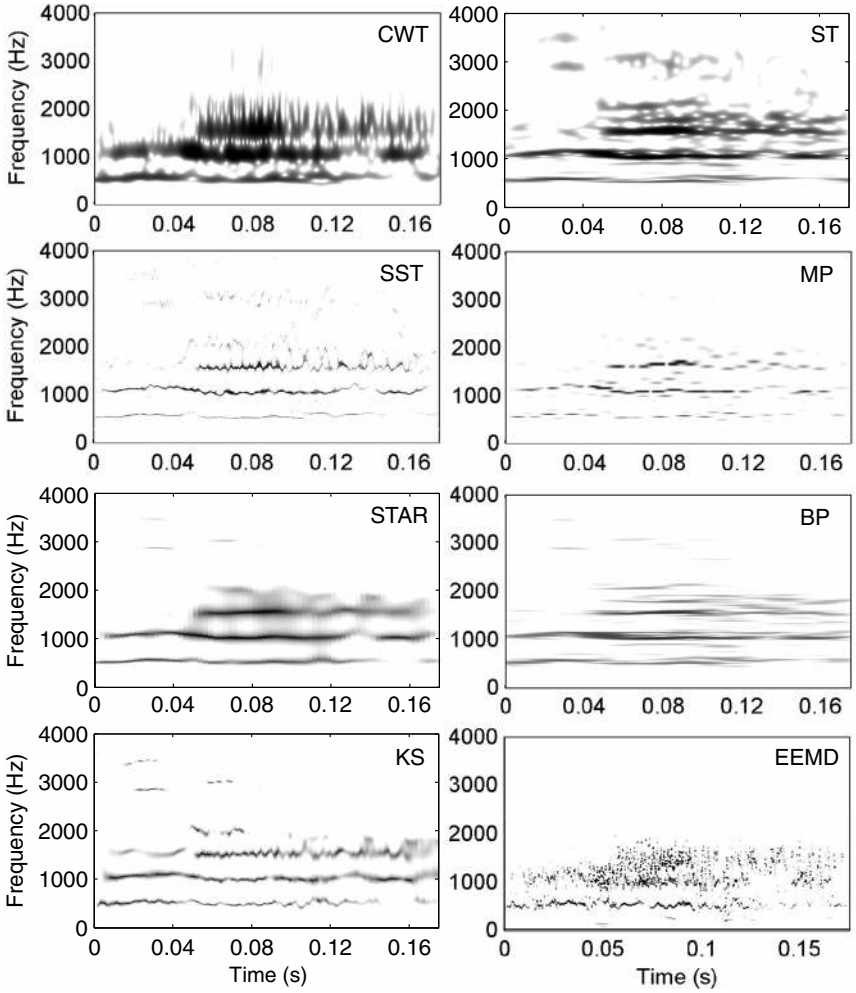

Figure 5. Time-frequency representations of the speech signal shown in Figure 4 using the ST, STAR, KS, CWT, SST, EMD, BP, and MP. The computing parameters are as follows: ST, parameter k=32; STAR, window of 0.025 s with 90% overlap and an autoregressive order of 14; KS, autoregressive order of 14; CWT and SST, Morlet wavelet with 64 voices per octave; EEMD, 100 realizations and random noise injection with 15% of the signal maximum amplitude; MP: Gabor dictionary; BP, Morlet wavelet dictionary and regularization parameter λ=0.5.

autoregressive coefficients are sometimes necessary to handle the appearance of frequency components over time.

The sparse representation imposed by the matching pursuit (MP) algorithm and the choice of the Gabor dictionary lead to discontinuous spectral lines and the localized mapping of the Morlet atom. We select the Morlet wavelet dictionary for analyzing the benchmark signals with basis pursuit which is very similar to the Gabor atoms dictionary used with matching pursuit [*Addison*, 2002]. The better performance of basis pursuit compared with matching pursuit is mainly due to the optimization scheme for finding the optimal solution in equation (18) ensuring sparsity of the solution [*Chen et al.*, 2001; *Vera Rodriguez et al.*, 2012]. Noticeably, the *t–f* representations of autoregressive methods, basis pursuit, synchrosqueezing transform, and ensemble empirical mode decomposition are not showing the differences in amplitude between the various signal components.

3.1.2. Seminal Example: Speech Signal

Spectral analysis is commonly used to characterize speech signal and for pattern recognition [*Rabiner and Juang*, 1993]. The different methods are applied to a short sample of a speech signal, specifically a laughing voice (Figure 4). The signal, sampled at 8000 Hz, is mainly composed of three harmonics at ~600, ~1050, and ~1570 Hz (Figure 5). Its signal-to-noise ratio (SNR), based on the maximum amplitude of the noise and the signal, is greater than 3.

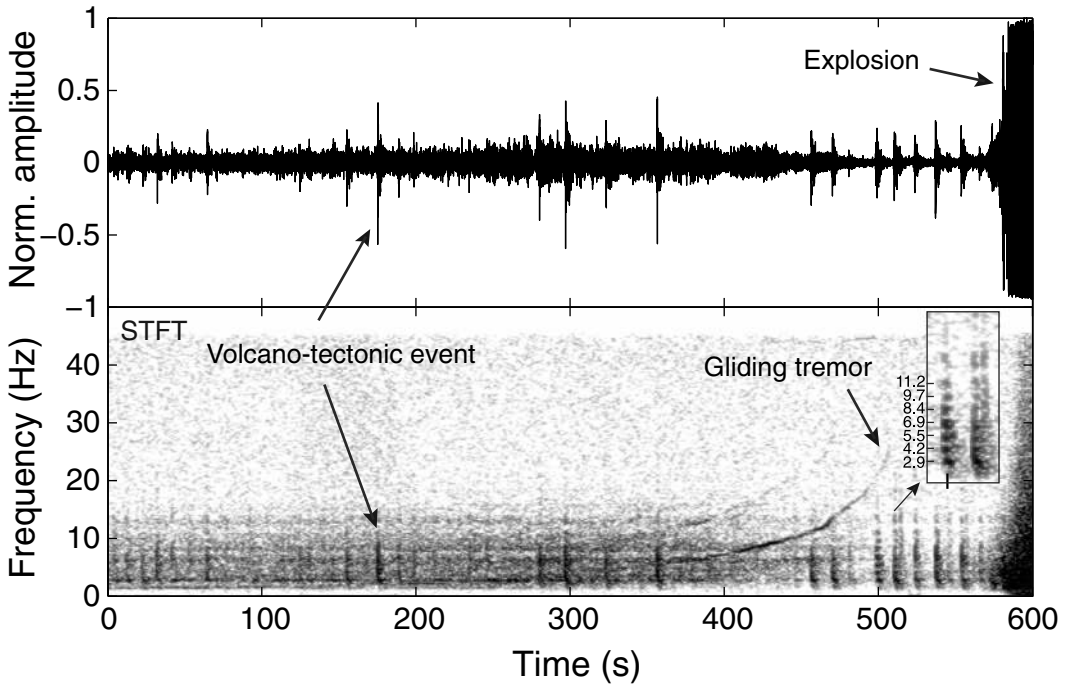

Figure 6. Volcanic pre-explosion recordings from the Redoubt volcano, Alaska [*Hotovec et al.*, 2013] (top), and time-frequency representation obtained using the STFT (bottom). The STFT is computed using a Hann taper of 5.12 s with 90% overlap. The inset is an enlargement of two volcano-tectonic events showing their main frequency components.

All techniques are able to pick up the three main spectral components. An additional low-amplitude spectral line is discernible around 2050 Hz only for some of the techniques, namely, the short-time Fourier transform, *S* transform, basis pursuit, short-time autoregressive method, and Kalman smoother. The decrease in frequency localization towards higher frequencies prevents the continuous wavelet transform and synchrosqueezing transform from detecting this low-amplitude spectral component. Even though the principle of the *S* transform is very similar to the continuous wavelet transform, the frequency localization has been adjusted using the parameter k (see equation (9)) to depict the low-amplitude line. Time-frequency representations of nonconventional methods (i.e., autoregressive methods, synchrosqueezing transform, empirical mode decomposition, matching pursuit, and basis pursuit) show less noise than the conventional methods, which are prone to smearing and leakage. The highest frequency components are however oscillating between 1000 and 1600 Hz for ensemble empirical mode decomposition and hence cannot be separated. For basis pursuit, the value of the regularization parameter λ is the same as for the synthetic signal (0.5) which gives approximately the same weight to data misfit and nonzero coefficients **a** in the cost function (equation (18)). This choice seems well adapted for the representation of spectral lines.

One can wonder if the rapid oscillations present in the synchrosqueezing transform and Kalman smoother decompositions correspond to the correct picture of the signal *t–f* content, as no other techniques show these oscillations. Comparing in detail the synchrosqueezing transform and Kalman smoother representations, we can see that most of these oscillations are similar in both pictures, especially for the spectral line around 1570 Hz. The fact that both techniques based on entirely different methodologies produce very close results likely means that these oscillations are indeed correct. Several reasons can explain why the other techniques are missing these rapid frequency modulations, smearing for the short-time Fourier transform, continuous wavelet transform and *S* transform, averaging over a relatively long window for the short-time autoregressive method, irregular fluctuations of instantaneous frequencies for ensemble empirical mode decomposition, sparsity, and size of the operator (i.e., atom family) for matching pursuit, and amount of smoothing in the inversion for basis pursuit. A high localization in both time and frequency is here the key to their detection.

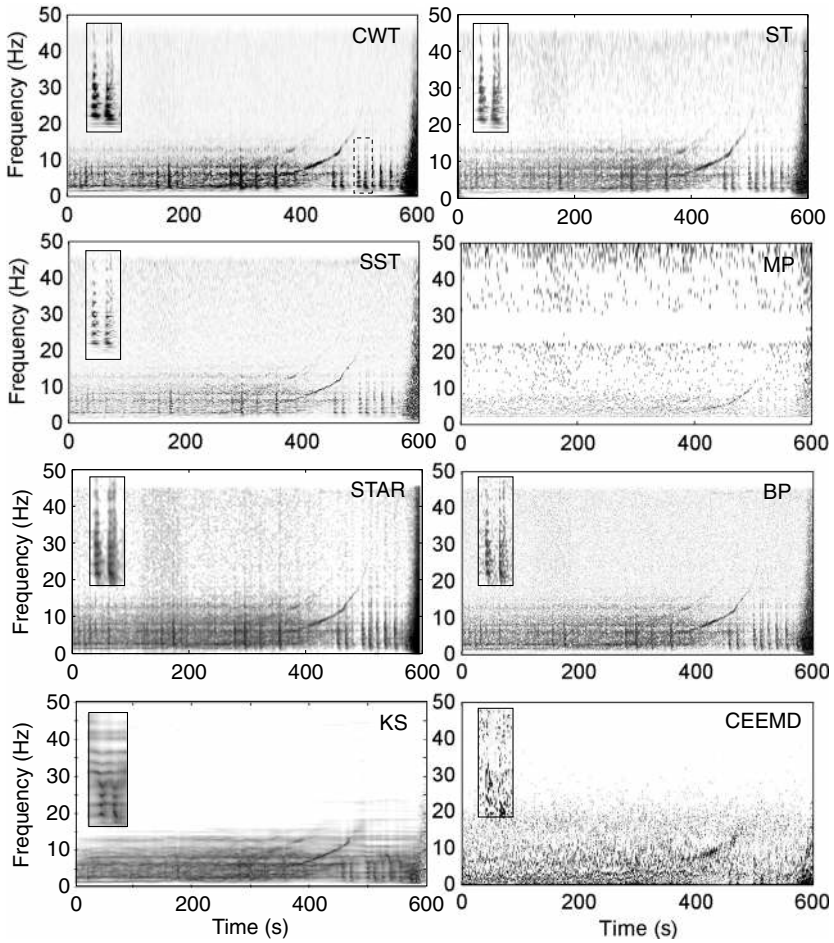

Figure 7. Time-frequency representations of the signal recorded at Redoubt volcano, Alaska (See Figure 6), using the ST, STAR, KS, CWT, SST, EMD, BP, and MP. It includes numerous volcano-tectonic earthquakes as well as a gliding tremor. The computing parameters are as follows: ST, parameter k=32; STAR, window of 6 s with 90% overlap and an autoregressive order of 97; KS, autoregressive order of 97; CWT and SST, Morlet wavelet with 32 voices per octave; CEEMD, 100 realizations and random noise injection with 10% of the signal maximum amplitude; MP, Gabor dictionary; BP, Morlet wavelet dictionary and regularization parameter $\lambda = 3$. Insets are enlargements of the same two volcano-tectonic events as those enlarged in Figure 6 for the STFT and indicated by the dashed rectangle in the CWT plot.

3.2. Geophysical Data Examples

3.2.1. Volcanic Tremor

Volcanic tremors are observed on many volcanoes worldwide [e.g., *Chouet*, 1996]. They distinguish themselves from their relatives, the long-period events, by the absence of strong onsets with broad spectra. They are characterized by long durations and harmonics mainly between 0.5 and 10 Hz. Potential causes range from the resonance of fluid-filled cracks [*Aki et al.*, 1977; *Frehner and Schmalholz*, 2010], nonlaminar flow in sinuous conduits [*Julian*, 1994; *Benson et al.*, 2008], or repetitive events with quasi-perfect periodicity [*Lees et al.*, 2004].

The tremor sample presented here was recorded in 2009 at Redoubt volcano, Alaska (event 12 in *Hotovec et al.* [2013]), by a short-period station (natural frequency 1–2 Hz, sampling frequency 100 Hz). This tremor was preceded by swarms of volcano-tectonic events with decreasing interevent periodicity and followed by an explosive episode in the volcano. The signal is constituted by one fundamental harmonic plus one overtone gliding toward higher frequencies over time, as well as numerous volcano-tectonic events and some broadband noise up to 15 Hz (Figure 6). *Hotovec et al.* [2013] suggest that the tremor cause is the repetition of periodic volcano-tectonic events with decreasing interevent periodicity owing to their large number before the tremor. *Hotovec et al.* [2013] note also that increasing the size of the signal window improves

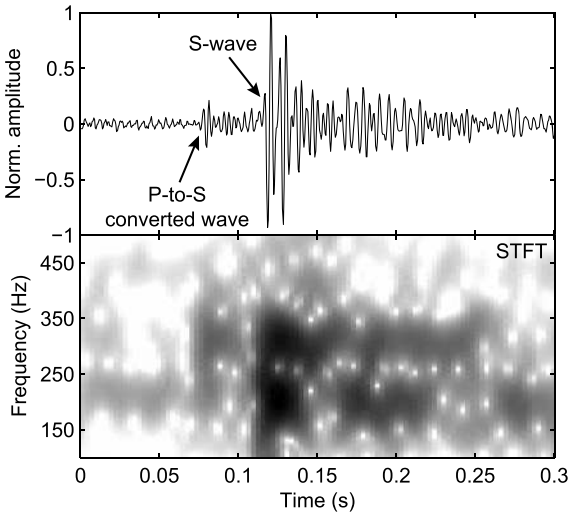

Figure 8. (top) Raw recordings and (bottom) time-frequency representation obtained with the STFT of a microseismic event recorded by a borehole geophone (vertical component) during a hydraulic fracturing treatment. Two seismic phases are indicated, a *P*-to-*S* converted wave, likely converted very close to the receiver, and the *S* wave. The STFT is computed using a Hann taper of 0.03 s with 90% overlap.

the readability of harmonics and overtones in short-time Fourier transform *t–f* decompositions, coming at the expense of time localization. This limitation of the short-time Fourier transform could be alleviated by some of the techniques presented in this study, such as autoregressive methods, empirical mode decomposition, basis pursuit, and the synchrosqueezing transform.

With this signal, the different techniques are challenged in terms of noise sensitivity and adaptability to different types of *t–f* signatures. Volcano-tectonic events have SNR ranging between ∼1 to 5, while the tremor is approximately at the noise level. The decomposition results are presented in Figures 6 and 7. Overall, conventional methods are performing similarly on this signal. The frequency content is mainly below 15 Hz, with the exceptions of the gliding tremor (from 365 s and 6.2 Hz to 507 s and 27 Hz) and its overtone (from 364 s and 11.7 Hz to 470 s and 28.6 Hz). Volcano-tectonic events correspond to the broad vertical lines with a frequency content mainly below 15 Hz. Some of them seem to consist of several frequency components (∼7), especially those after the appearance of the gliding tremor. This feature is better seen on the *t–f* representations of the *S* transform, continuous wavelet transform, synchrosqueezing transform, basis pursuit and short-time autoregressive method (Figure 7).

On the other hand, no significant improvements are achieved by the nonconventional techniques for the delineation of the gliding tremors compared with the conventional ones. The *t–f* picture for the short-time Fourier transform presented in Figure 6 has a higher frequency localization than the one presented in *Hotovec et al.* [2013], even though the same window size was used. The main parameters to improve the short-time Fourier transform resolution and readability are the window size, the type of taper used, and the number of points of the Fourier transform. The good performances of the continuous wavelet transform on this signal are transferred to the synchrosqueezing transform, which shows the highest *t–f* localization of all techniques.

The high-amplitude noise degrades the performance of complete ensemble empirical mode decomposition (CEEMD) technique such that the tremor and the volcano-tectonic events are not, or barely, identifiable before and after around 400 s, respectively. The noise also degrades the representation of this signal by matching pursuit due to the absence of a separation mechanism between signal and noise components in this algorithm. The iterative procedure and the compromise entrusted to the regularization parameter λ, which is equal to 3 for this signal, enable basis pursuit to reduce contributions from the noise.

The spectral localization as well as the performance of both autoregressive methods depends on the SNR [*Marple*, 1982; *Quirk and Liu*, 1983]; this is particularly clear on the *t–f* representation of the Kalman smoother. For the present signal, a high autoregressive order is needed to account for the broadband character of the volcano-tectonic events and the background noise. The autoregressive methods are fitting peaked spectra to these broadband frequency components, leading to the horizontally hatched aspect of this Kalman smoother representation.

Both the short-time Fourier transform and continuous wavelet transform represent well broad continuous spectra, whereas autoregressive methods, the synchrosqueezing transform, and empirical mode decomposition try to condense such spectra to a few single frequencies [*Kay and Marple*, 1981; *Auger et al.*,

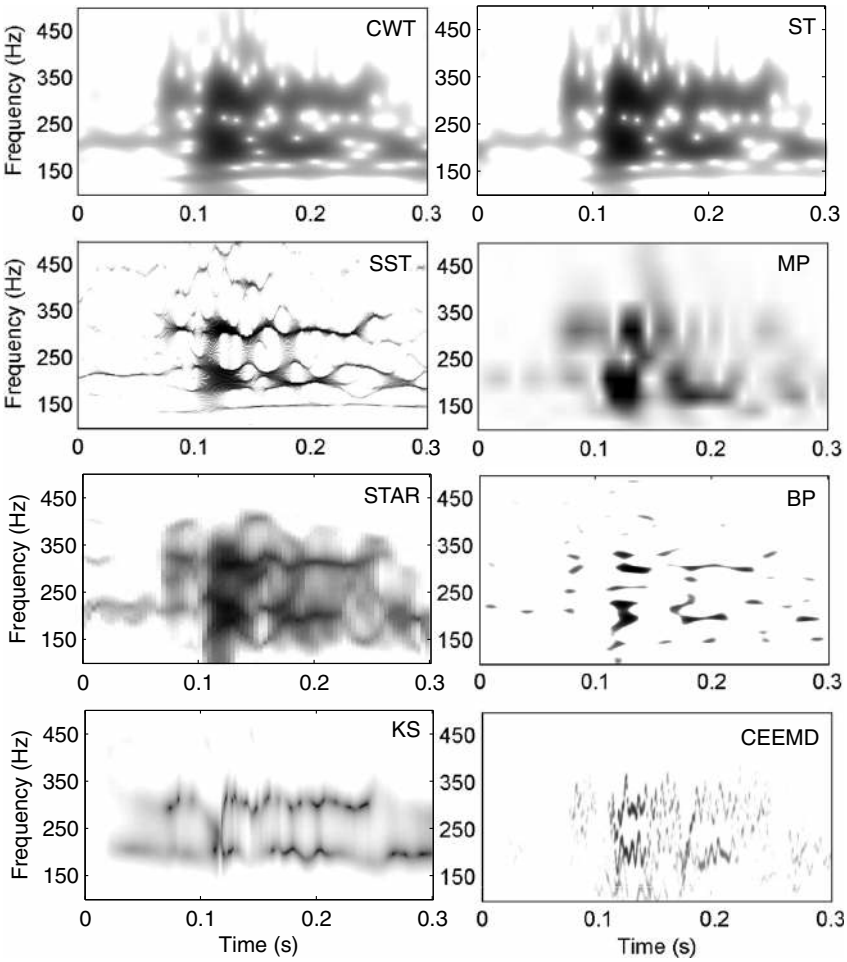

Figure 9. Time-frequency representations of the microseismic event in Figure 8), using the ST, STAR, KS, CWT, SST, EMD, BP, and MP. The computing parameters are as follows: ST, parameter $k = 4$; STAR, window of 0.04 s with 90% overlap and an autoregressive order of 11; KS, autoregressive order of 11; CWT and SST, Morlet wavelet with 64 voices per octave; CEEMD, 100 realizations and random noise injection with 15% of the signal maximum amplitude; MP, Gabor dictionary; BP, Morlet wavelet dictionary and regularization parameter $\lambda = 0.05$.

2013; *Mandic et al.*, 2013]. Hence, they display the gliding tremor fairly well but not necessarily the volcano-tectonic events.

3.2.2. Microseismic Event

Microseismic events are small brittle failure events occurring when fluids are injected inside a rock volume, be it for enhanced oil recovery, geothermal operations, or carbon capture and storage for example. These events are usually recorded by geophones deployed in boreholes to decrease surface noise contamination and be closer to the point of fluid injection into the reservoir. Their magnitude are usually negative, ranging from −3 to −1 [*Cipolla et al.*, 2011]. The *t–f* representation of these events is complicated mainly by their very short durations generally between 0.1 and 1 s. A clear separation of the different seismic phases is then difficult to obtain due to the limits in time and frequency localizations of conventional *t–f* methods [*Herrera et al.*, 2015].

In this section, we analyze a high-quality microseismic event recorded during a 24-stage hydraulic fracturing experiment that took place in Rolla, British Columbia, Canada, in 2011 [*Eaton et al.*, 2013]. The fracturing is monitored by a toolstring of six downhole short-period geophones, with a sampling frequency of 2000 Hz. The signal shown in Figure 8 corresponds to the recordings of a magnitude −1.7 microseismic event by the vertical component of the deepest geophone. Its SNR is superior to 1.5 allowing an easy identification of two wave arrivals. The two wavepackets correspond to a *P*-to-*S* converted wave, likely converted close to

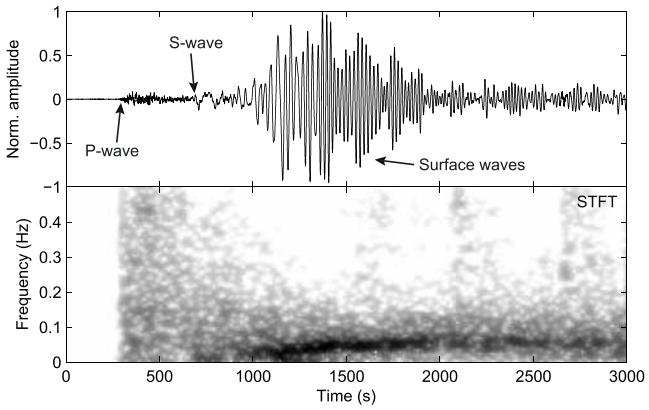

Figure 10. (top) Raw recordings and (bottom) time-frequency representation obtained with the STFT of the M_w9 Tohoku earthquake by the broad-band station KDAK (vertical component) of the IRIS IDA network. The main seismic phases are also indicated. The STFT is computed using a Hann taper of 100 s with 90% overlap.

the receiver location, and the *S* wave. On the short-time Fourier transform picture (Figure 8), the converted wave has a frequency content around 320 Hz while the S-wave consists of two main components at 320 and 210 Hz.

The *t–f* representations of this microseismic event are presented in Figures 8 and 9. Due to the short signal window imposed by the short duration of these kind of events, the picture of conventional methods suffers heavily from spectral smearing and the different components are spread out over a frequency interval of approximately 50 Hz. Apart from matching pursuit and basis pursuit, the other nonconventional methods are converting the different zones into several localized lines. The synchrosqueezing transform, basis pursuit, Kalman smoother, and complete ensemble empirical mode decomposition representations offer the best performance in terms of time and frequency localizations, the short-time autoregressive method representation being noisier.

On the other hand, Kalman smoother and complete ensemble empirical mode decomposition representations show rapid amplitude modulations, together with frequency modulations for complete ensemble empirical mode decomposition, which are not corroborated by the other representations. Matching pursuit clearly localizes the main three frequency components but show higher smearing than the other nonconventional methods. The basis pursuit algorithm detects approximately the same components but focus them around their central frequencies. The regularization parameter λ used for this signal is equal to 0.05 which is favoring the reduction of data misfit over the number of nonzero coefficients **a**. Matching pursuit, basis pursuit, and complete ensemble empirical mode decomposition are able to represent the monofrequency tails in the event coda between 0.15 and 0.3 s.

3.2.3. Megathrust Earthquake: Tohoku 2011, M_w9

The M_w9 Tohoku earthquake occurred on 11 March 2011, offshore the northwest coast of Japan where the Pacific plate subducts under the Okhotsk plate [*Tajima and Kennett*, 2012]. The seismogram presented in Figure 10 was recorded by the borehole station KDAK from the IRIS IDA network located in Kodiak Island on the Aleutian trench, South Alaska. This station has a three-component broadband seismometer with sampling frequency at 20 Hz giving an usable frequency band between around 0.003 and 10 Hz. The main signal from the earthquake lasts for about half an hour, with a high SNR superior to 10.

The *t–f* representations of this seismogram using the presented techniques are given in Figures 10 and 11. *P* waves arrive at ∼265 s and have a broadband frequency content up to the Nyquist frequency (not shown in figures). *S* waves, arriving at ∼695 s, have a more localized frequency content around 0.015 Hz. The late high-amplitude arrival corresponds to surface waves. Their dispersion curve is clearly visible on the *t–f* representations, starting from around 0.02 Hz at 1115 s to reach 0.05 Hz at later times.

The broadband character of the *P* waves gives to the short-time Fourier transform and *S* transform representations a blurry aspect. Together with the continuous wavelet transform representation, they show some smearing around the dispersion curve of the surface waves. While the *S* wave arrival is discernible on the short-time Fourier transform and continuous wavelet transform representations, this is not the case for the *S* transform. This arrival is actually also visible only on complete ensemble empirical mode decomposition and perhaps the short-time autoregressive method, Kalman smoother, and basis pursuit *t–f* plots (Figure 11). Except for the short-time autoregressive method, nonconventional techniques elude the *P* waves arrival with its broad spectrum in their *t–f* representations.

The surface waves are well characterized by the nonconventional techniques, especially the synchrosqueezing transform and Kalman smoother. The matching pursuit technique shows the dispersion curve relatively

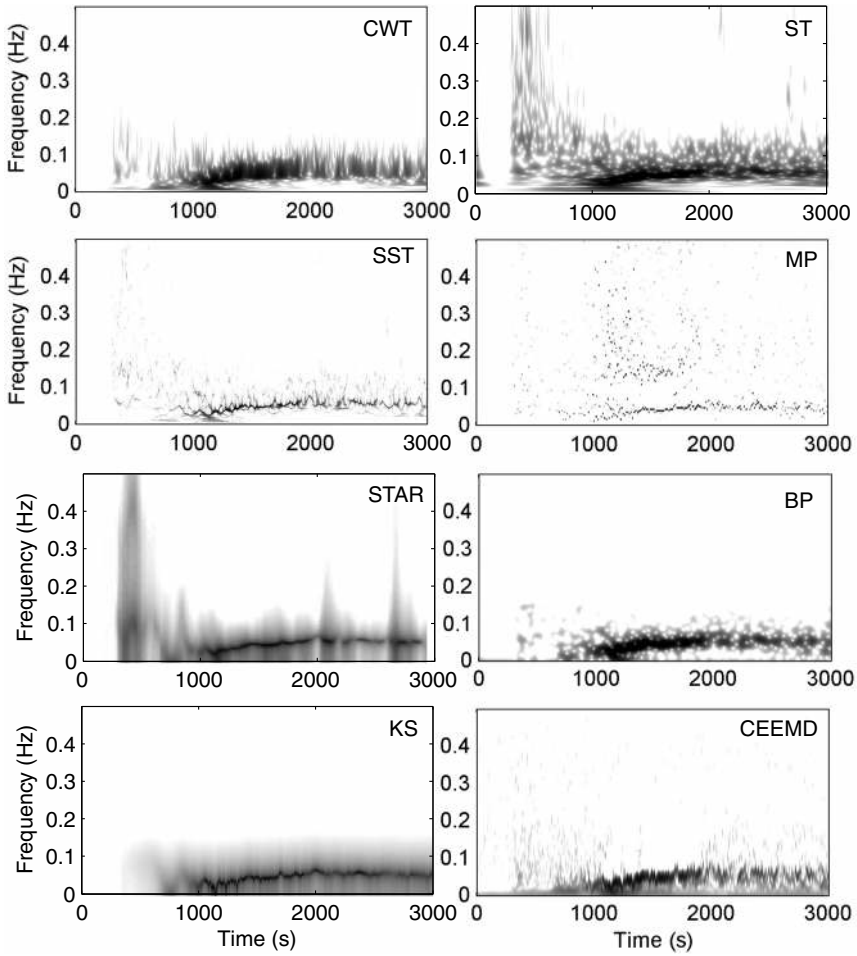

Figure 11. Time-frequency representations of the M_w9 Tohoku earthquake recorded by station KDAK (vertical component) of the IRIS network (See Figure 10), using the ST, STAR, KS, CWT, SST, EMD, BP, and MP. The computing parameters are as follows: ST, parameter $k = 4$; STAR, window of 150 s with 90% overlap and an autoregressive order of 6; KS, autoregressive order of 6; CWT and SST, Bump wavelet with 64 voices per octave; CEEMD, 100 realizations and random noise injection with 10% of the signal maximum amplitude; MP, Ricker dictionary; BP, Morlet wavelet dictionary and regularization parameter $\lambda = 1$.

well, even though it seems that this method has more difficulties to delineate time-varying spectral lines, as previously seen also on the synthetic signal (Figure 3). The high amplitude of the surface waves allows for an easy recovery of this component by autoregressive methods, even with a low number of autoregressive coefficients (six autoregressive coefficients in Figure 11).

4. Discussion

Table 2 gives the key parameters, a summary of the main *t–f* features, and the main references for each *t–f* technique.

4.1. Parametrization and Adaptability

Depending on the *t–f* template, or an *a priori* model, the resulting *t–f* representations will be very contrasting as illustrated by the presented applications. Obtained *t–f* estimates are then not "absolute" measures but actually reflect the contents of their template. All techniques are however able to decompose and fully reconstruct the signal under investigation, given some basis, with the exception of autoregressive methods which are appropriate only for peaked spectra. The fact that these transforms are fully reversible indicates that they all lead to correct *t–f* representations. However, one method might provide more insight into a particular signal than another one. Results from different techniques should be compared in order to

Table 2. Summary of Key *t–f* Parameters and Features for the *t–f* Techniques Presented in This Review[a]

Techniques	Key Parameters	Key *t–f* Features	Main References
STFT	Window length and overlap, taper type, number of frequency bins	Fixed *t–f* resolution, smearing of $t-f$ components	*Cohen* [1989]
CWT	Type of mother wavelet and its central frequency, number of voices and octaves	Variable *t–f* resolution, exponential frequency axis, smearing of *t–f* components	*Daubechies* [1992] and *Kumar and Foufoula-Georgiou* [1997]
ST	Localization parameter *k*, number of frequency bins	Variable *t–f* resolution, linear frequency axis, smearing of *t–f* components	*Stockwell et al.* [1996] and *Reine et al.* [2009]
SST	Same as CWT plus computation of instantaneous frequencies and reassignment	Reassignment of CWT *t–f* distribution on the instantaneous frequencies ridges leading to narrow-band frequency components	*Daubechies et al.* [2011], *Thakur et al.* [2013], and *Herrera et al.* [2014]
MP	Dictionary definition, algorithm stopping criterion	Sparse *t–f* representations, deflationary approach potentially leading to non optimum $t-f$ decompositions	*Mallat and Zhang* [1993] and *Wang* [2007]
BP	Dictionary definition, regularization parameter λ	Sparse *t–f* representations, inversion scheme leading to locally optimum *t–f* decompositions	*Chen et al.* [2001] and *Vera Rodriguez et al.* [2012]
STAR	Autoregressive order, window length and overlap, autoregressive method	Peaked spectra, no windowing and hence smearing reduction	*Makhoul* [1975], *Kay and Marple* [1981], and *Leonard and Kennett* [1999]
KS	Autoregressive order, parameters for the training data set (noise amplitude, number of realizations)	Smoother peaked spectra, time-varying autoregressive coefficients	*Khan and Dutt* [2007] and *Tary et al.* [2014]
EMD	Stopping criteria for IMFs extraction, extrema interpolation algorithm	Computation of instantaneous frequencies from IMFs, narrow-band and fluctuating frequency components, problems of mode mixing and splitting, aliasing, end-points artefacts	*Huang et al.* [1998], *Flandrin et al.* [2004], and *Bekara and Van der Baan* [2009]
EEMD	Same as EMD plus amplitude of Gaussian white noise injected and number of realizations	Same as EMD but reduces mode mixing and aliasing, possibility of IMFs mixing in the frequency domain and incomplete decomposition of the signal	*Wu and Huang* [2009], *Mandic et al.* [2013], and *Tong et al.* [2012]
CEEMD	Same as EEMD	Same as EEMD without IMFs mixing in the frequency domain, complete decomposition of the signal	*Torres et al.* [2011] and *Han and van der Baan* [2013]

[a]IMF, intrinsic mode function.

gain confidence on their *t–f* decomposition, particularly for techniques that are strongly model dependent (e.g., matching and basis pursuits and autoregressive methods). While the various *t–f* techniques are more or less suitable for different kind of signals, these techniques can also serve two main rationales which are time series representation and time series manipulation [*Auger et al.*, 2013].

In addition, the presented techniques not only rely on different assumptions such as periodicity or peaked spectra but also on the determination on various parameters that are critical for the *t–f* picture. The necessary parameters depend on the technique considered. For the short-time Fourier transform, four main parameters influence the *t–f* representation: window size, taper type, overlap, and number of frequency bins in the fast Fourier transform [*Harris*, 1978; *Kay and Marple*, 1981]. Wavelet- and dictionary-based techniques both depend on the choice of the basis atom (Morlet, Ricker, bump wavelets, etc.), even though techniques exist to estimate this basis atom from the data themselves [*Mesa*, 2005], or to merge several dictionaries into a "super-dictionary" [*Chen et al.*, 2001; *Rubinstein et al.*, 2010]. Additional parameters affect the *t–f* decomposition such as the number of octaves and voices for the continuous wavelet transform [*Daubechies*, 1992] and the regularization parameter for basis pursuit [*Vera Rodriguez et al.*, 2012]. As the synchrosqueezing transform depends on the continuous wavelet transform results, it is governed by the same parameters plus those for instantaneous frequencies computation [*Thakur et al.*, 2013].

The main parameters for empirical mode decomposition are the stopping criteria for the sifting process and the extrema interpolation scheme (splines in this study) [*Han and van der Baan*, 2013; *Mandic et al.*, 2013]. For the different examples presented in the application section, ensemble empirical mode decomposition and complete ensemble empirical mode decomposition employed with the same parameters show similar

t–f representations. On the other hand, the ensemble empirical mode decomposition implementation tends to extract smoother IMFs with increasing IMF numbers due to the decrease in Gaussian noise fluctuations, which is not the case in the complete ensemble empirical mode decomposition implementation. From our tests, complete ensemble empirical mode decomposition is more computationally intensive than ensemble empirical mode decomposition which contradicts the conclusions of *Torres et al.* [2011]. We show ensemble empirical mode decomposition results when no significant improvement is achieved by using complete ensemble empirical mode decomposition.

Autoregressive methods mainly depend mainly on the autoregressive order. If the autoregressive order is too low, then the spectrum will be very smooth and some spectral peaks will be lost or misplaced, whereas if the autoregressive order is too high, then spurious peaks can appear and spectral line splitting can occur [*Kay and Marple*, 1981]. Various methods have been proposed to determine the autoregressive order, such as spectral comparison [*Tary et al.*, 2014], information theory-based criteria (e.g., Akaike information criterion, final prediction error) [*Priestley*, 1994] which weigh the misfit of the model with the data against the model complexity and higher order statistics [*Lesage*, 2008]. In the case of signal with noise, information theory criteria usually do not converge toward an optimum value but decrease with increasing autoregressive orders. However, the curve of Akaike information criterion against autoregressive order can be useful to determine when no significant improvements are made by increasing the autoregressive order and hence find the optimum order. The other methods provide an autoregressive order that seem to give reasonable results.

The various techniques show different levels of adaptability to all possible time series. Techniques that are based on a fixed basis (e.g., mother wavelet and dictionaries) or present strong model assumptions are naturally less adjustable to different kinds of signals than techniques completely data driven such as empirical mode decomposition. On the downside, empirical mode decomposition algorithm seems very sensitive to the SNR as no criterion to separate noise and signal is defined in this kind of algorithm. At the same time, empirical mode decomposition coupled with the Hilbert-Huang spectrum, which involves the computation of instantaneous frequencies, seems to limit its *t–f* representation potential to narrow-band signals, as illustrated by the broadband signals of the Tohoku mega-earthquake (Figure 11) and the Redoubt volcano (Figure 7).

Algorithms of conventional methods for *t–f* analysis (short-time Fourier transform, continuous wavelet transform, *S* transform) show more adaptability to different spectral bandwidths owing to the flexibility of their templates. A complete representation of the *t–f* content of a signal, including narrow-band and broadband components, is achieved by the conventional techniques at the cost of a lower time-frequency localization. Nonconventional techniques all rely on various assumptions to increase their localization or separating power, at the expense of "rejecting" parts of the signal. The biggest challenge is then to obtain an adaptable technique with both high time and frequency localizations. None of the presented techniques succeeds unequivocally in this task, even though the basis pursuit and synchrosqueezing transform give promising results.

4.2. Performances

Conventional methods, subject to the uncertainty principle, present some smearing for all examples, especially in the case of the microseismic event (Figure 9). The *S* transform performances are also limited by the total number of samples of the signal N as the resulting *t–f* array will have a size $N \times N$. Allowing a lower number of frequencies, like for the fast Fourier transform, and decimating the signal in time can help reduce the size of the *t–f* array. Matching pursuit performances are found to be generally lower than those of the other methods, including the conventional ones. The sparse representation of matching pursuit might be inadequate for the applications shown in this study. On the other hand, matching pursuit may be more suitable for signal compression. Conversely, basis pursuit shows that "superlocalization" achieved by sparsity constrained inversion is appropriate for most of the examples shown in this study. In addition, the compromise between data misfit and sparsity through the resolution parameter λ increases the flexibility of this technique.

The reassignment method applied on instantaneous frequencies for the synchrosqueezing transform improves the *t–f* representation of the continuous wavelet transform in all the examples shown. However, some limitations of the continuous wavelet transform, such as the exponential frequency sampling, that sometimes compromises its *t–f* representations are then transferred to the *t–f* pictures of the

synchrosqueezing transform. Empirical mode decomposition and variants ensemble empirical mode decomposition and complete ensemble empirical mode decomposition offer high-localized *t–f* representation for signals characterized by good SNR (e.g., the microseismic event, surface waves of the Tohoku earthquake). On the other hand, instantaneous frequencies computed from empirical mode decomposition IMFs have an inconsistent aspect in the presence of high-amplitude broadband noise (e.g., Redoubt volcano example) and for close spectral lines (e.g., speech signal) [see also *Bowman and Lees*, 2013]. In these contexts, instantaneous frequencies calculated from the continuous wavelet transform picture (synchrosqueezing transform) show a more continuous aspect, expected for these geophysical and audio signals, and lower noise sensitivity. Finally, instantaneous frequencies, if coupled with decomposition into subsignals like the synchrosqueezing transform and empirical mode decomposition, may be the paradigm of the ultimate frequency localization, but examples like the *P* and *S* waves arrivals of Tohoku mega-earthquake seem to indicate that some natural signals with broadband spectra are not well represented by instantaneous frequencies.

Autoregressive methods are shown to be particularly efficient for spectral line delineation, for the speech signal or the dispersion curve of surface waves for example. For the Kalman smoother method, a careful attention should be given to potential spurious frequency components (e.g., synthetic signal), and poor *t–f* pictures are obtained for signals with low SNR (e.g., Redoubt volcano example). These methods combine high time-frequency localization with an absence of smearing, leading to clearer *t–f* representation over conventional techniques. Improvements obtained by using autoregressive methods are more significant for signals with high SNR [*Marple*, 1982]. This could explain the relative absence of improvements for the Redoubt volcano signal (Figure 7).

All considered methods allow for signal reconstruction. In this review, we focus on signal representation, not signal manipulation. The fact that all methods permit reconstruction indicates that they all can be used for signal manipulation. We anticipate that their suitability for manipulation could be quite different from the visual impression provided by their signal representation.

4.3. Possible Improvements

An automatic, data-driven selection of the main parameters for the continuous wavelet transform (mother wavelet, central frequency, and bandwidth) [*Mesa*, 2005] could be combined with the synchrosqueezing transform algorithm in order to remove the usual trial-and-error procedure. This could also improve the resulting *t–f* representation of the continuous wavelet transform. On the other hand, the continuous wavelet transform could be replaced by another time-frequency decomposition such as the curvelet transform [*Yang and Ying*, 2014] or the *S* transform. The latter shows equal or better performances than the continuous wavelet transform and also requires less tunable parameters. Data-driven selection of the right dictionary could also improve the performance of methods such as matching pursuit and basis pursuit [*Hou and Shi*, 2011].

The selection of the optimal autoregressive order is a longstanding issue for autoregressive methods that is left open. Autoregressive methods relying on stochastic estimates usually involve high computational costs that limit their real-time implementation. Modern computational tools and programming languages should help mitigate this problem; this is also true for other methods like empirical mode decomposition and variants.

Algorithms imposing sparsity on their *t–f* decomposition, such as constrained inversion schemes [*Vera Rodriguez et al.*, 2012], might increase their *t–f* localization in an artificial way for broad-band signals. In other words, these signals have a broad spectrum which is compacted by the decomposition method, providing in essence an incorrect representation. Hence, there is a need for algorithms that can handle both narrowband and broadband *t–f* representations depending on the actual underlying signal characteristics. In a similar way as the synchrosqueezing transform is combining the continuous wavelet transform, instantaneous frequencies, and reassignment in a single method, mixing algorithms [e.g., *Puryear et al.*, 2012] or dictionaries [e.g., *Rubinstein et al.*, 2010] might be alternatives to address these important challenges.

Finally, all considered algorithms in this review are single-trace and thus one-dimensional methods. However, multidimensional signals are very common (e.g., photos and shot gathers in reflection seismology). Likewise, multicomponent data are also abundant. In a multicomponent recording, different types of signals are recorded at the same spatial position and time (e.g., three-component seismic signals, omni-directional

microphones, and red-green-blue channels in photos). Many of the presented methods have their multidimensional counterparts including multidimensional wavelet transforms [*Kumar and Foufoula-Georgiou*, 1997], 2-D empirical mode decomposition [*Nunes and Deléchelle*, 2009], and multidimensional autoregressive models [*McClellan*, 1982; *Hansen and Chellappa*, 1988]. Both matching pursuit and basis pursuit can easily be extended to handle multidimensional signals too [*Bergeaud and Mallat*, 1995; *Chen et al.*, 2001; *Mendels et al.*, 2007; *Bruckstein et al.*, 2009].

We anticipate that many of the other novel high-localization methods will also be transformed to higher dimensions. The topic of high-localization multicomponent spectral analysis has however received relatively less attention for geophysical applications, despite its practical importance. Generally, each component is decomposed separately (e.g., the vertical component in a seismic section or the red channel in a photo) and subsequently individually or jointly analyzed. Ideally however, multicomponent, multidimensional data should be decomposed jointly, instead of individually, with a single algorithm. We nevertheless anticipate new developments in this area such that signal characteristics present on one or more recorded components can be successfully jointly decomposed and subsequently analyzed instead of trying to infer their presence from the individual component decompositions. The recent introduction of the quaternion-based Fourier transform offers much promise to achieve multicomponent, multidimensional decompositions [*Ell and Sangwine*, 2007].

5. Conclusion

Time-frequency analysis is a cornerstone of geophysical signal analysis. Close examination of the theoretical basis of the presented conventional and nonconventional techniques reveals their assumptions and restrictions. These also often determine their time-frequency localization. Conventional techniques, i.e., the short-time Fourier transform, continuous wavelet transform, and *S* transform, are based on a quantitative comparison of the signal with a template. This is also true for some of the nonconventional techniques like matching pursuit and basis pursuit, while the synchrosqueezing transform actually combines it with instantaneous frequencies determination and the reassignment method. Other nonconventional techniques are directly based on data modeling such as autoregressive methods and empirical mode decomposition and variants.

The applications to a synthetic signal, a speech signal, and various geophysical time series show the capabilities of the various techniques in terms of their adaptability to different frequency content, time-frequency localization, and noise sensitivity. Conventional techniques perform similarly on the various signals, clearly showing their main shortcomings which are spectral smearing and the trade-off between time and frequency localizations. The nonconventional techniques address them more or less efficiently in different ways. Out of all the presented techniques, the synchrosqueezing transform and basis pursuit are the only one providing high-localization and low noise sensitivity, even though the synchrosqueezing transform results are broadly dictated by those of the continuous wavelet transform. Matching pursuit and basis pursuit results are also bound by the suitability of the dictionary to the analyzed signal. Kalman smoother and empirical mode decomposition show high time-frequency localizations but also a high sensitivity to the signal-to-noise ratio. The actual performance of each technique is then ultimately conferred by their original design (e.g., matching pursuit for signal compression and autoregressive method for time series prediction).

Recent developments like data-driven procedures (empirical mode decomposition), algorithmic combinations (synchrosqueezing transform), or inversion schemes (basis pursuit) show potential ways to improve time-frequency representations. They might hold the keys to help circumvent longstanding hurdles such as the high-localization representation of both narrow-band and broadband spectra at the same time.

Acknowledgments

The authors would like to thank the sponsors of the Microseismic Industry consortium for financial support, and Arc Resources, Spectraseis, Nanometrics, and ESG Solutions are thanked for their support of the field project of the Rolla experiment. We acknowledge the IRIS consortium which was used for access to waveform and metadata of the KDAK and REF stations of the IRIS IDA and AV networks, respectively. All benchmark signals are provided as supplementary materials to this review. We thank the Editor-in-Chief and Matt Hall for their thorough reviews which improved the quality of this review. The authors of the original codes for some techniques are also greatly acknowledged. For the synchrosqueezing transform, the code uses the main functions of the synchrosqueezing transform toolbox (https://web.math.princeton.edu/~ebrevdo/synsq/). For the Kalman smoother, the main routines are adapted from those of M.E. Khan (http://www.cs.ubc.ca/~emtiyaz/publications.html). Empirical mode decomposition codes are modified from those of P. Flandrin (http://perso.ens-lyon.fr/patrick.flandrin/emd.html), and M.E. Torres (http://bioingenieria.edu.ar/grupos/ldnlys/metorres/re_inter.htm). The source codes for the basis pursuit technique were kindly provided by M. Sacchi, D. Bonar, and I. Vera Rodriguez.

The Editor on this paper was Fabio Florindo. He thanks Matt Hall and one anonymous reviewer.

References

Addison, P. S. (2002), *The Illustrated Wavelet Transform Handbook: Introductory Theory and Applications in Science, Engineering, Medicine and Finance*, IOP, Bristol, U. K.

Aki, K., M. Fehler, and S. Das (1977), Source mechanism of volcanic tremors: Fluid-driven crack model and their application to the 1963 Kilauea eruption, *J. Volcanol. Geotherm. Res.*, *2*(3), 259–287.

Auger, F., and P. Flandrin (1995), Improving the readability of time-frequency and time-scale representations by the reassignment method, *IEEE Trans. Signal Process.*, *43*(5), 1068–1089.

Auger, F., P. Flandrin, Y.-T. Lin, S. McLaughlin, S. Meignen, T. Oberlin, and H.-T. Wu (2013), Time-frequency reassignment and synchrosqueezing: An overview, *IEEE Signal Process. Mag.*, *30*(6), 32–41, doi:10.1109/MSP.2013.2265316.

Barnes, A. (2007), A tutorial on complex seismic trace analysis, *Geophysics*, *72*(6), W33–W43, doi:10.1190/1.2785048.

Barnhart, B. L., and W. E. Eichinger (2011), Analysis of sunspot variability using the Hilbert–Huang transform, *Sol. Phys.*, *269*, 439–449, doi:10.1007/s11207-010-9701-6.
Baziw, E., and I. Weir-Jones (2002), Application of kalman filtering techniques for microseismic event detection, *Pure Appl. Geophys.*, *159*, 449–471.
Beck, A., and M. Teboulle (2009), A fast iterative shrinkage-thresholding algorithm for linear inverse problems, *SIAM J. Imaging Sci.*, *2*(1), 183–202, doi:10.1137/080716542.
Bekara, M., and M. Van der Baan (2009), Random and coherent noise attenuation by empirical mode decomposition, *Geophysics*, *74*(5), V89–V98, doi:10.1190/1.3157244.
Benson, P. M., S. Vinciguerra, P. G. Meredith, and R. P. Young (2008), Laboratory simulation of volcano seismicity, *Science*, *322*, 249–252.
Bergeaud, F., and S. Mallat (1995), Matching pursuit of images, *Proc. IEEE Int. Conf. Image Process.*, *1*, 53–56, doi:10.1109/ICIP.1995.529037.
Bertino, L., G. Evensen, and H. Wackernagel (2003), Sequential data assimilation techniques in oceanography, *Int. Stat. Rev.*, *71*, 223–241, doi:10.1111/j.1751-5823.2003.tb00194.x.
Bolton, E. W., K. A. Maasch, and J. M. Lilly (1995), A wavelet analysis of Plio-Pleistocene climate indicators: A new view of periodicity evolution, *Geophys. Res. Lett.*, *22*(20), 2753–2756, doi:10.1029/95GL02799.
Bonar, D., and M. Sacchi (2010), Complex spectral decomposition via inversion strategies, *SEG Annu. Meeting Abstr.*, 1408–1412, doi:10.1190/1.3513105.
Bowman, D. C., and J. M. Lees (2013), The Hilbert–Huang transform: A high resolution spectral method for nonlinear and nonstationary time series, *Seismol. Res. Lett.*, *84*(6), 1074–1080, doi:10.1785/0220130025.
Brigham, E. O. (1988), *The Fast Fourier Transform and Its Applications, Signal Processing Series*, Prentice-Hall, Englewood Cliffs, N. J.
Bruckstein, A., D. Donoho, and M. Elad (2009), From sparse solutions of systems of equations to sparse modeling of signals and images, *SIAM Rev.*, *51*(1), 34–81.
Burg, J. P. (1972), The relationship between maximum entropy spectra and maximum likelihood spectra, *Geophysics*, *37*, 375–376.
Cazelles, B., M. Chavez, D. Berteaux, F. Ménard, J. O. Vik, S. Jenouvrier, and N. C. Stenseth (2008), Wavelet analysis of ecological time series, *Oecologia*, *156*(2), 287–304, doi:10.1007/s00442-008-0993-2.
Chen, S. S., D. L. Donoho, and M. A. Saunders (2001), Atomic decomposition by basis pursuit, *SIAM Rev.*, *43*(1), 129–159.
Chen, W. Y., and G. R. Stegen (1974), Experiments with maximum entropy power spectra of sinusoids, *J. Geophys. Res.*, *79*(20), 3019–3022, doi:10.1029/JB079i020p03019.
Chouet, B. A. (1996), Long-period volcano seismicity: Its source and use in eruption forecasting, *Nature*, *380*, 309–316.
Cipolla, C., S. Maxwell, M. Mack, and R. Downie (2011), A practical guide to interpreting microseismic measurements, paper presented at SPE-144067-MS International Conference, Soc. Pet. Eng., The Woodlands, Tex., 14-16 June.
Cohen, L. (1989), Time-frequency distributions—A review, *Proc. IEEE*, *77*(7), 941–981.
Cooley, J. W., and J. W. Tukey (1965), An algorithm for the machine calculation of complex Fourier series, *Math. Comput.*, *19*(90), 297–301.
Cooley, J. W., P. A. W. Lewis, and P. D. Welch (1969), The fast fourier transform and its applications, *IEEE Trans. Educ.*, *12*(1), 27–34.
Daubechies, I. (1992), *Ten Lectures on Wavelets, CBMS-NSF Regional Conference Series in Applied Mathematics*, vol. 61, Soc. for Indust. and Appl. Math. (SIAM), Philadelphia, Pa.
Daubechies, I., J. Lu, and H.-T. Wu (2011), Synchrosqueezed wavelet transforms: An empirical mode decomposition-like tool, *Appl. Comput. Harmonic Anal.*, *30*(2), 243–261, doi:10.1016/j.acha.2010.08.002.
Dikpati, M., J. L. Anderson, and D. Mitra (2014), Ensemble Kalman filter data assimilation in a Babcock-Leighton solar dynamo model: An observation system simulation experiment for reconstructing meridional flow speed, *Geophys. Res. Lett.*, *41*, 5361–5369, doi:10.1002/2014GL061077.
Eaton, D., M. van der Baan, J. B. Tary, B. Birkelo, N. Spriggs, S. Cutten, and K. Pike (2013), Broadband microseismic observations from a Montney hydraulic fracture treatment, northeastern B.C., Canada, *CSEG Recorder*, *38*(3), 44–53.
Ell, T. A., and S. J. Sangwine (2007), Hypercomplex Fourier transforms of color images, *IEEE Trans. Image Process.*, *16*, 22–35.
Farge, M. (1992), Wavelet transforms and their applications to turbulence, *Annu. Rev. Fluid Mech.*, *24*(1), 395–457, doi:10.1146/annurev.fluid.24.1.395.
Figueiredo, M., R. Nowak, and S. Wright (2007), Gradient projection for sparse reconstruction: Application to compressed sensing and other inverse problems, *IEEE J. Sel. Top. Signal Process.*, *1*(12), 568–598.
Flandrin, P., G. Rilling, and P. Gonçalvés (2004), Empirical mode decomposition as a filter bank, *IEEE Signal Process. Lett.*, *11*, 112–114.
Fomel, S. (2007), Local seismic attributes, *Geophysics*, *72*(3), A29–A33, doi:10.1190/1.2437573.
Frehner, M., and S. M. Schmalholz (2010), Finite-element simulations of Stoneley guided-waves reflection and scattering at the tips of fluid-filled fractures, *Geophysics*, *75*(2), T23–T36, doi:10.1190/1.3340361.
Gabor, D. (1946), Theory of communication, *J. Inst. Electr. Eng.*, *93*(26), 429–457, doi:10.1049/ji-3-2.1946.0074.
Gao, R., R. Yan, and SpringerLink (2010), *Wavelets: Theory and Applications for Manufacturing*, Springer, Bücher, New York.
Ghil, M., et al. (2002), Advanced spectral methods for climatic time series, *Rev. Geophys.*, *40*(1), 1003, doi:10.1029/2000RG000092.
Grewal, M. S., and A. P. Andrews (2001), *Kalman Filtering: Theory and Practice Using MATLAB,* 2nd ed., Wiley-Intersci., New York.
Hall, M. (2006), Resolution and uncertainty in spectral decomposition, *First Break*, *24*, 43–47, doi:10.3997/1365-2397.2006027.
Hall, M. G., A. V. Oppenheim, and A. S. Willsky (1983), Time-varying parametric modeling of speech, *Signal Process.*, *5*, 267–285.
Han, J., and M. van der Baan (2013), Empirical mode decomposition for seismic time-frequency analysis, *Geophysics*, *78*(2), O9–O19, doi:10.1190/geo2012-0199.1.
Han, L., M. D. Sacchi, and L. Han (2014), Spectral decomposition and de-noising via time-frequency and space-wavenumber reassignment, *Geophys. Prospect.*, *62*(2), 244–257, doi:10.1111/1365-2478.12088.
Hansen, R. R., Jr., and R. Chellappa (1988), Two-dimensional robust spectrum estimation, *IEEE Trans. Acoust. Speech Signal Process.*, *36*(7), 1051–1066, doi:10.1109/29.1628.
Harris, F. (1978), On the use of windows for harmonic analysis with the discrete Fourier transform, *Proc. IEEE*, *66*(1), 51–83, doi:10.1109/PROC.1978.10837.
Herrera, R. H., J. Han, and M. van der Baan (2014), Applications of the synchrosqueezing transform in seismic time-frequency analysis, *Geophysics*, *79*(3), V55–V64, doi:10.1190/geo2013-0204.1.
Herrera, R. H., J. B. Tary, M. van der Baan, and D. W. Eaton (2015), Body wave separation in the time-frequency domain, *IEEE Geosci. Remote Sens. Lett.*, *12*(2), 364–368, doi:10.1109/LGRS.2014.2342033.
Hinich, M. J., and C. S. Clay (1968), The application of the discrete fourier transform in the estimation of power spectra, coherence, and bispectra of geophysical data, *Rev. Geophys.*, *6*(3), 347–363.
Hotovec, A. J., S. G. Prejean, J. E. Vidale, and J. Gomberg (2013), Strongly gliding harmonic tremor during the 2009 eruption of Redoubt Volcano, *J. Volcanol. Geotherm. Res.*, *259*, 89–99.

Hou, T. Y., and Z. Shi (2011), Adaptive data analysis via sparse time-frequency representation, *Adv. Adaptive Data Anal.*, *3*(1), 1–28.
Huang, N. E., Z. Shen, S. R. Long, M. C. Wu, H. H. Shih, Q. Zheng, N.-C. Yen, C. C. Tung, and H. H. Liu (1998), The empirical mode decomposition and the Hilbert spectrum for nonlinear and non-stationary time series analysis, *Proc. R. Soc. London A*, *454*, 903–995, doi:10.1098/rspa.1998.0193.
Julian, B. R. (1994), Volcanic tremor: Nonlinear excitation by fluid flow, *J. Geophys. Res.*, *99*(B6), 11,859–11,877.
Kaipio, J. P., and P. A. Karjalainen (1997), Estimation of event-related synchronization changes by a new TVAR method, *IEEE Trans. Biomed. Eng.*, *44*, 649–656.
Kay, S., and S. Marple (1979), Sources of and remedies for spectral line splitting in autoregressive spectrum analysis, *IEEE Int. Conf. ICASSP Acoustics Speech Signal Process.*, *4*, 151–154.
Kay, S., and S. Marple (1981), Spectrum analysis—A modern perspective, *Proc. IEEE*, *69*(11), 1380–1419, doi:10.1109/PROC.1981.12184.
Khan, M. E., and D. N. Dutt (2007), An expectation-maximization algorithm based kalman smoother approach for event-related desynchronization (ERD) estimation from EEG, *IEEE Trans. Biomed. Eng.*, *54*, 1191–1198.
Kravchinsky, V. A., C. G. Langereis, S. D. Walker, K. G. Dlusskiy, and D. White (2013), Discovery of Holocene millennial climate cycles in the Asian continental interior: Has the sun been governing the continental climate?, *Global Planet. Change*, *110*, 386–396, doi:10.1016/j.gloplacha.2013.02.011.
Kumar, P., and E. Foufoula-Georgiou (1997), Wavelet analysis for geophysical applications, *Rev. Geophys.*, *35*(4), 385–412, doi:10.1029/97RG00427.
Labat, D. (2005), Recent advances in wavelet analyses: Part 1. A review of concepts, *J. Hydrol.*, *314*(1–4), 275–288, doi:10.1016/j.jhydrol.2005.04.003.
Lees, J. M., E. I. Gordeev, and M. Ripepe (2004), Explosions and periodic tremor at Karymsky volcano, Kamchatka, Russia, *Geophys. J. Int.*, *158*(3), 1151–1167.
Leonard, M., and B. L. N. Kennett (1999), Multi-component autoregressive techniques for the analysis of seismograms, *Phys. Earth Planet. Int.*, *113*, 247–263.
Lesage, P. (2008), Automatic estimation of optimal autoregressive filters for the analysis of volcanic seismic activity, *Nat. Hazards Earth Syst. Sci.*, *8*, 369–376.
Li, C., and M. Liang (2012), A generalized synchrosqueezing transform for enhancing signal time-frequency representation, *Signal Process.*, *92*(9), 2264–2274, doi:10.1016/j.sigpro.2012.02.019.
Magrin-Chagnolleau, I., and R. Baraniuk (1999), Empirical mode decomposition based time-frequency attributes, *Proc. 69th SEG Meeting*, 1949–1952.
Makhoul, J. (1975), Spectral linear prediction: Properties and applications, *IEEE Trans. Acoust. Speech Signal Process.*, *23*(3), 283–296.
Mallat, S. (2008), *A Wavelet Tour of Signal Processing, The Sparse Way,* 3rd ed., Acad. Press, Burlington, Mass.
Mallat, S., and Z. Zhang (1993), Matching pursuits with time-frequency dictionaries, *IEEE Trans. Signal Process.*, *41*(12), 3397–3415, doi:10.1109/78.258082.
Mandic, D. P., R. U. Rehman, Z. Wu, and N. E. Huang (2013), Empirical mode decomposition-based time-frequency analysis of multivariate signals: The power of adaptive data analysis, *IEEE Signal Process. Mag.*, *30*(6), 74–86, doi:10.1109/MSP.2013.2267931.
Marple, S. L. J. (1982), Frequency resolution of Fourier and maximum entropy spectral estimates, *Geophysics*, *47*(9), 1303–1307.
McClellan, J. H. (1982), Multidimensional spectral estimation, *Proc. IEEE*, *70*(9), 1029–1039.
Mendels, F., P. Vandergheynst, and J.-P. Thiran (2007), Matching pursuit-based shape representation and recognition using scale-space, *Int. J. Imaging Syst. Technol.*, *16*, 162–180, doi:10.1002/ima.20078.
Mesa, H. (2005), Adapted wavelets for pattern detection, in *Progress in Pattern Recognition, Image Analysis and Applications, Lecture Notes in Computer Science*, vol. 3773, pp. 933–944, Springer, Berlin, Heidelberg.
Miyahara, H., K. Masuda, Y. Muraki, H. Kitagawa, and T. Nakamura (2006), Variation of solar cyclicity during the Spoerer Minimum, *J. Geophys. Res.*, *111*, A03103, doi:10.1029/2005JA011016.
Muthuswamy, J., and N. V. Thakor (1998), Spectral analysis methods for neurological signals, *J. Neurosci. Methods*, *83*, 1–14.
Nunes, J.-C., and E. Deléchelle (2009), Empirical mode decomposition: Applications on signal and image processing, *Adv. Adapt. Data Anal.*, *1*(1), 125–175, doi:10.1142/S1793536909000059.
Priestley, M. B. (1994), *Spectral Analysis and Time Series*, Acad. Press, London, U. K.
Puryear, C. I., O. N. Portniaguine, C. M. Cobos, and J. P. Castagna (2012), Constrained least-squares spectral analysis: Application to seismic data, *Geophysics*, *77*(5), V143–V167, doi:10.1190/geo2011-0210.1.
Quirk, M., and B. Liu (1983), *On the Resolution of Autoregressive Spectral Estimation*, IEEE ICASSP, Boston, Mass.
Rabiner, L., and B.-H. Juang (1993), *Fundamentals of Speech Recognition*, Prentice Hall, Englewood Cliffs, N. J.
Rauch, H. E., C. T. Striebel, and F. Tung (1965), Maximum likelihood estimates of linear dynamic systems, *AIAA J.*, *3*, 1445–1450.
Reager, J. T., B. F. Thomas, and J. S. Famiglietti (2014), River basin flood potential inferred using GRACE gravity observations at several months lead time, *Nat. Geosci.*, *7*, 588–592, doi:10.1038/ngeo2203.
Reine, C., M. van der Baan, and R. Clark (2009), The robustness of seismic attenuation measurements using fixed- and variable-window time-frequency transforms, *Geophysics*, *74*, WA123–WA135, doi:10.1190/1.3043726.
Rioul, O., and M. Vetterli (1991), Wavelets and signal processing, *IEEE Signal Process. Mag.*, *8*(4), 14–38, doi:10.1109/79.91217.
Rubinstein, R., A. M. Bruckstein, and M. Elad (2010), Dictionaries for sparse representation modeling, *Proc. IEEE*, *98*(6), 1045–1057, doi:10.1109/JPROC.2010.2040551.
Salisbury, J. I., and M. Wimbush (2002), Using modern time series analysis techniques to predict ENSO events from the SOI time series, *Nonlinear Process. Geophys.*, *9*, 341–345, doi:10.5194/npg-9-341-2002.
Segall, P., E. K. Desmarais, D. Shelly, A. Miklius, and P. Cervelli (2006), Earthquakes triggered by silent slip events on Kilauea volcano, Hawaii, *Nature*, *442*, 71–74, doi:10.1038/nature04938.
Stockwell, R. G. (2007), Why use the S-transform?, in *Pseudo-Differential Operators: Partial Differential Equations and Time-Frequency Analysis, Fields Institute Communications*, vol. 52, edited by L. Rodino, B.-W. Schulze, and M. W. Wong, pp. 279–309, Am. Math. Soc., Toronto, Ontario, Canada.
Stockwell, R. G., L. Mansinha, and R. P. Lowe (1996), Localization of the complex spectrum: The S-transform, *IEEE Trans. Signal Process.*, *44*(4), 998–1001, doi:10.1109/78.492555.
Tajima, F., and B. L. N. Kennett (2012), Interlocking of heterogeneous plate coupling and aftershock area expansion pattern for the 2011 Tohoku-Oki Mw9 earthquake, *Geophys. Res. Lett.*, *39*, L05307, doi:10.1029/2011GL050703.
Taner, M. T., F. Koehler, and R. E. Sheriff (1979), Complex seismic trace analysis, *Geophysics*, *44*(11), 1041–1063.
Tary, J. B., R. H. Herrera, and M. van der Baan (2014), *Time-Varying Autoregressive Model for Spectral Analysis of Microseismic Experiments and Long-Period Events*, *196*(1), 600–611, doi:10.1093/gji/ggt400.

Thakur, G., E. Brevdo, N. S. Fučkar, and H.-T. Wu (2013), The Synchrosqueezing algorithm for time-varying spectral analysis: Robustness properties and new paleoclimate applications, *Signal Process.*, *93*(5), 1079–1094, doi:10.1016/j.sigpro.2012.11.029.

Tong, W., Z. Mingcai, Y. Qihao, and Z. Huyuan (2012), Comparing the applications of EMD and EEMD on time-frequency analysis of seismic signal, *J. Appl. Geophys.*, *83*, 29–34, doi:10.1016/j.jappgeo.2012.05.002.

Torrence, C., and G. P. Compo (1998), A practical guide to wavelet analysis, *Bull. Am. Meteorol. Soc.*, *79*(1), 61–78.

Torres, M., M. Colominas, G. Schlotthauer, and P. Flandrin (2011), A complete ensemble empirical mode decomposition with adaptive noise, in *IEEE International Conference on Acoustics, Speech and Signal Processing (ICASSP)*, pp. 4144–4147, IEEE, Prague, Czech Republic.

Ulrych, T. J., and T. N. Bishop (1975), Maximum entropy spectral analysis and autoregressive decomposition, *Rev. Geophys. Space Phys.*, *13*(1), 183–200.

Ulrych, T. J., and M. Ooe (1983), *Autoregressive and Mixed Autoregressive-Moving Average Models and Spectra*, Springer, Berlin, Germany.

van den Berg, E., and M. P. Friedlander (2008), Probing the Pareto frontier for basis pursuit solutions, *SIAM J. Sci. Comput.*, *31*(2), 890–912, doi:10.1137/080714488.

Vera Rodriguez, I., D. Bonar, and M. D. Sacchi (2012), Microseismic data denoising using a 3C group sparsity constrained time-frequency transform, *Geophysics*, *77*, V21–V29, doi:10.1190/geo2011-0260.1.

Walker, G. T. (1931), On periodicity in series of related terms, *Proc. R. Soc. London Ser. A*, *131*, 518–532.

Wang, Y. (2007), Seismic time-frequency spectral decomposition by matching pursuit, *Geophysics*, *72*(1), V13–V20, doi:10.1190/1.2387109.

Wold, H. (1938), *A Study in the Analysis of Stationary Time Series*, Almquist and Wiksell, Stockholm, Sweden.

Wu, Z., and N. E. Huang (2009), Ensemble empirical mode decomposition: A noise-assisted data analysis method, *Adv. Adapt. Data Anal.*, *1*(1), 1–41.

Yang, H., and L. Ying (2014), Synchrosqueezed curvelet transform for Two-dimensional mode decomposition, *SIAM J. Math. Anal.*, *46*(3), 2052–2083.

Yule, G. U. (1927), On a method of investigating periodicities in disturbed series, with special reference to Wolfer's sunspot numbers, *Philos. Trans. R. Soc. London Ser. A*, *226*, 267–298.

Zhang, R., and J. Castagna (2011), Seismic sparse-layer reflectivity inversion using basis pursuit decomposition, *Geophysics*, *76*(6), R147–R158, doi:10.1190/geo2011-0103.1.